J. Fluid Mech. (2013), *vol.* 719, *pp.* 14–46.
doi:10.1017/jfm.2012.596

Optimal Taylor–Couette flow: direct numerical simulations

Rodolfo Ostilla[1,†], Richard J. A. M. Stevens[1,2], Siegfried Grossmann[3], Roberto Verzicco[1,4] and Detlef Lohse[1]

[1]Department of Science and Technology, Mesa+ Institute and J. M. Burgers Centre for Fluid Dynamics, University of Twente, P.O. Box 217, 7500 AE Enschede, The Netherlands

[2]Department of Mechanical Engineering, Johns Hopkins University, 3400 N. Charles Street, Baltimore, MD 21218, USA

[3]Department of Physics, University of Marburg, Renthof 6, D-35032 Marburg, Germany

[4]Dipartimento di Ingegneria Meccanica, University of Rome 'Tor Vergata', Via del Politecnico 1, Roma 00133, Italy

(Received 4 July 2012; revised 22 November 2012; accepted 29 November 2012; first published online 19 February 2013)

We numerically simulate turbulent Taylor–Couette flow for independently rotating inner and outer cylinders, focusing on the analogy with turbulent Rayleigh–Bénard flow. Reynolds numbers of $Re_i = 8 \times 10^3$ and $Re_o = \pm 4 \times 10^3$ of the inner and outer cylinders, respectively, are reached, corresponding to Taylor numbers Ta up to 10^8. Effective scaling laws for the torque and other system responses are found. Recent experiments with the Twente Turbulent Taylor–Couette (T^3C) setup and with a similar facility in Maryland at very high Reynolds numbers have revealed an optimum transport at a certain non-zero rotation rate ratio $a = -\omega_o/\omega_i$ of about $a_{opt} = 0.33$. For large enough Ta in the numerically accessible range we also find such an optimum transport at non-zero counter-rotation. The position of this maximum is found to shift with the driving, reaching a maximum of $a_{opt} = 0.15$ for $Ta = 2.5 \times 10^7$. An explanation for this shift is elucidated, consistent with the experimental result that a_{opt} becomes approximately independent of the driving strength for large enough Reynolds numbers. We furthermore numerically calculate the angular velocity profiles and visualize the different flow structures for the various regimes. By writing the equations in a frame co-rotating with the outer cylinder a link is found between the local angular velocity profiles and the global transport quantities.

Key words: convection, direct numerical simulation, Taylor–Couette flow

1. Introduction

Taylor–Couette (TC) flow, i.e. the flow in the gap between two independently rotating coaxial cylinders, is among the most investigated problems in fluid mechanics, due to its conceptional simplicity and to applications in process technology, see e.g. Haim & Pismen (1994). Traditionally, the driving of this system is expressed by the Reynolds numbers of the inner and outer cylinders, defined by $Re_i = r_i\omega_i d/\nu$ and $Re_o = r_o\omega_o d/\nu$, where r_i and r_o are the inner and outer cylinder radius,

† Email address for correspondence: R.Ostillamonico@utwente.nl

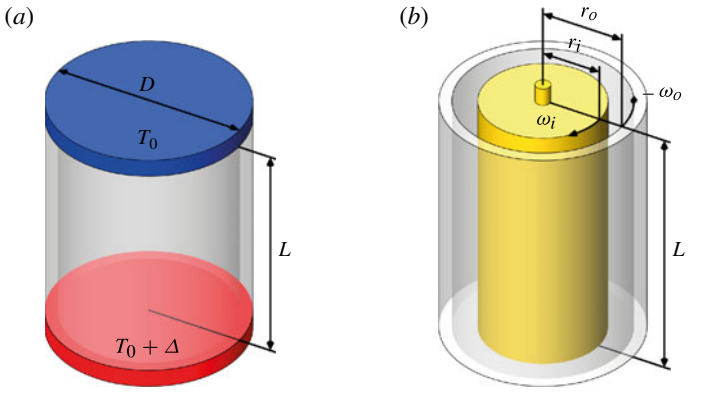

FIGURE 1. (Colour online) Geometry of the Rayleigh–Bénard (*a*) and the Taylor–Couette systems (*b*). The RB system consists of two cylindrical plates, a hot one at the bottom and a cold one at the top of diameter D separated by a distance L. The top plate is at a temperature T_0 and the bottom plate is at a temperature $T_0 + \Delta$, with Δ the temperature difference between the plates. The TC system consists of two coaxial cylinders of length L. The inner cylinder has the radius r_i and the angular velocity ω_i, while the outer cylinder has the radius r_o and the angular velocity ω_o.

respectively, $d = r_o - r_i$ is the gap width, ω_i and ω_o the angular velocities of the inner and outer cylinders, and ν the kinematic viscosity. In dimensionless numbers the geometry of a TC system is expressed by the radius ratio $\eta = r_i/r_o$ and the aspect ratio $\Gamma = L/d$, see figure 1. In the limit $\eta \to 1$, the flow becomes plane Couette flow. It was shown by Eckhardt, Grossmann & Lohse (2007) (from now on referred to as EGL 2007) that TC flow has many similarities to Rayleigh–Bénard (RB) convection, i.e. the thermal flow in a fluid layer heated from below and cooled from above, which will be discussed in detail below.

Both RB and TC flows have been popular playgrounds for the development of new concepts in fluid dynamics. Both systems have been used to study instabilities (Busse 1967; Chandrasekhar 1981; Drazin & Reid 1981; Pfister & Rehberg 1981; Pfister *et al.* 1988), nonlinear dynamics and chaos (Lorenz 1963; Ahlers 1974; Behringer 1985; Strogatz 1994), pattern formation (Andereck, Liu & Swinney 1986; Cross & Hohenberg 1993; Bodenschatz, Pesch & Ahlers 2000), and turbulence (Lathrop, Fineberg & Swinney 1992*b*; Siggia 1994; Grossmann & Lohse 2000; Kadanoff 2001; Ahlers, Grossmann & Lohse 2009; Lohse & Xia 2010). The reasons that RB and TC are so popular include: (i) these systems are mathematically well-defined by the Navier–Stokes equations and the appropriate boundary conditions; (ii) these are closed systems and thus exact global balance relations between the driving and the dissipation can be derived; and (iii) they are experimentally and numerically accessible with high precision, thanks to the simple geometries and high symmetries.

The analogy between TC and RB may be better seen from the exact relations (EGL 2007) between the transport quantities and the energy dissipation rates. For RB flow the conserved quantity that is transported is the thermal flux $J = \langle u_z \Theta \rangle_{A,t} - \kappa \partial_z \langle \Theta \rangle_{A,t}$ of the temperature field Θ, where κ is the thermal conductivity of the flow. The first term is then the convective contribution (u_z is the vertical fluid velocity component) and the second term is the diffusive contribution. Here $\langle \ldots \rangle_{A,t}$ indicates the averaging over time and a horizontal plane. In the state with lowest thermal driving there is not yet convection. Therefore $J \equiv J_0 = \kappa \Delta L^{-1}$ and the corresponding

Rayleigh–Bénard		Taylor–Couette	
Conserved: temperature flux		Conserved: angular velocity flux	
$J = \langle u_z \Theta \rangle_{A,t} - \kappa \partial_z \langle \Theta \rangle_{A,t}$	(1.3)	$J^\omega = r^3(\langle u_r \omega \rangle_{A,t} - \nu \partial_r \langle \omega \rangle_{A,t})$	(1.4)
Dimensionless transport:		Dimensionless transport:	
$Nu = \dfrac{J}{J_0}$	(1.5)	$Nu_\omega = \dfrac{J^\omega}{J_0^\omega} \left(= \dfrac{\tau}{2\pi L \rho J_0^\omega} \right)$	(1.6)
$J_0 = \kappa \Delta L^{-1}$	(1.7)	$J_0^\omega = \nu \dfrac{2 r_i^2 r_o^2}{r_i + r_o} \dfrac{\omega_i - \omega_o}{d}$	(1.8)
Driven by:		Driven by:	
$Ra = \dfrac{\beta g \Delta L^3}{\kappa \nu}$	(1.9)	$Ta = \dfrac{1}{4} \dfrac{\sigma\,(r_o - r_i)^2\,(r_i + r_o)^2\,(\omega_i - \omega_o)^2}{\nu^2}$	(1.10)
Exact relation:		Exact relation:	
$\tilde{\epsilon}'_u = \tilde{\epsilon}_u - \tilde{\epsilon}_{u,0}$	(1.11)	$\tilde{\epsilon}'_u = \tilde{\epsilon}_u - \tilde{\epsilon}_{u,0}$	(1.12)
$= (Nu - 1) Ra\, Pr^{-2}$	(1.13)	$= (Nu_\omega - 1) Ta\, \sigma^{-2}$	(1.14)
$\tilde{\epsilon}_{u,0} = 0$	(1.15)	$\tilde{\epsilon}_{u,0} = \dfrac{d^4}{\nu^3} \cdot \nu \dfrac{r_i^2 r_o^2}{r_a^2} \left(\dfrac{\omega_i - \omega_o}{d} \right)^2$	(1.16)
Prandtl number:		Pseudo 'Prandtl' number:	
$Pr = \nu / \kappa$	(1.17)	$\sigma = \left(1 + \dfrac{r_i}{r_o} \right)^4 \Big/ \left(4 \dfrac{r_i}{r_o} \right)^2$	(1.18)
Scaling:		Scaling:	
$Nu \propto Ra^\gamma$	(1.19)	$Nu_\omega \propto Ta^\gamma$	(1.20)

TABLE 1. Analogous relations between RB and TC flow, leading to the same effective scaling laws as derived by Eckhardt, Grossmann & Lohse (2007). In RB flow, the dimensionless control parameters are the Rayleigh number $Ra = \beta g \Delta L^3/(\nu\kappa)$, the Prandtl number $Pr = \nu/\kappa$, and the aspect ratio $\Gamma = D/L$, where Δ is the temperature difference between the cold top and hot bottom, β the thermal expansion coefficient, g the gravitational acceleration, and κ the thermal diffusivity, see figure 1. The response of the system is the heat flux from the bottom to the top in terms of the molecular heat flux, known as the Nusselt number Nu. In analogy, for TC flow we define a Nusselt number Nu_ω as ratio of the total and the purely azimuthal and laminar angular velocity flow. $\tilde{\epsilon}_{u,0}$ is the dissipation in the purely diffusive state, equal to zero in RB flow, since the fluid velocity is zero and there is molecular heat transport only, while in TC flow $\tilde{\epsilon}_{u,0}$ is the purely azimuthal and laminar flow dissipation rate.

dissipation rate is $\epsilon_{u,0} = 0$ since $\boldsymbol{u} = 0$. In TC flow, the conserved transport quantity, which is transported from the inner to the outer cylinder (or vice versa) is the flux $J^\omega = r^3(\langle u_r \omega \rangle_{A,t} - \nu \partial_r \langle \omega \rangle_{A,t})$ of the angular velocity field ω, where the first term is the convective contribution with u_r as the radial fluid velocity component and the second term is the diffusive contribution, cf. EGL (2007). In this case $\langle \ldots \rangle_{A,t}$ indicates averaging over time and a cylindrical surface with constant radial distance r from the axis. In the state with lowest driving induced by the rotating cylinders and neglecting effects from the upper and lower plates (achieved in the simulations by periodic boundary conditions in the axial direction), the flow is laminar and purely azimuthal, $u_\theta(r) = Ar + B/r$, while $u_r = u_z = 0$. This flow provides an angular velocity current J_0^ω (called J_{lam}^ω in EGL 2007) and a non-zero dissipation rate, see (1.8) and (1.16) in table 1.

The analogy between RB and TC (EGL 2007) is highlighted when the driving in TC is expressed in terms of the Taylor number Ta and the angular velocity ratio $a = -\omega_o/\omega_i$ of the cylinders, while the response is given by the dimensionless transport current density J^ω divided by the corresponding molecular current density of the angular velocity from the inner to the outer cylinder, called the 'ω-Nusselt number' Nu_ω. The Taylor number is defined as $Ta = \sigma\,(r_o - r_i)^2\,(r_o + r_i)^2\,(\omega_o - \omega_i)^2\,/(4\nu^2)$, or

$$Ta = (r_a^6 d^2/r_o^2 r_i^2 \nu^2)\,(\omega_o - \omega_i)^2\,. \tag{1.1}$$

Here

$$\sigma = r_a^4/r_g^4 \tag{1.2}$$

with $r_a = (r_o + r_i)/2$ the arithmetic and $r_g = \sqrt{r_o r_i}$ the geometric mean radii. $\omega_{o,i}$ are the angular velocities of the outer and inner cylinders, respectively; see also table 1 for definitions and relations.

TC flow has been extensively investigated experimentally (Wendt 1933; Taylor 1936; Smith & Townsend 1982; Andereck *et al.* 1986; Tong *et al.* 1990; Lathrop, Fineberg & Swinney 1992*a*; Lathrop *et al.* 1992*b*; Lewis & Swinney 1999; van Gils *et al.* 2011*a*,*b*; Paoletti & Lathrop 2011; Huisman *et al.* 2012) at low and high Ta for different ratios of the rotation frequencies $a = -\omega_o/\omega_i$, see the phase diagram in figure 3. However, up to now most numerical simulations of TC flow have been restricted to the case of pure inner-cylinder rotation (Fasel & Booz 1984; Coughlin & Marcus 1996; Dong 2007, 2008; Pirro & Quadrio 2008), or eigenvalue study (Gebhardt & Grossmann 1993), or counter-rotation at fixed a (Dong 2008). Recent experiments (van Gils *et al.* 2011*a*,*b*; Paoletti & Lathrop 2011; Huisman *et al.* 2012) have shown that at fixed Ta an optimal transport is obtained at non-zero a: van Gils *et al.* (2011*b*) obtained $a_{opt} = 0.33 \pm 0.05$, whereas Paoletti & Lathrop (2011) found $a_{opt} \approx 0.33$.

In this paper we use direct numerical simulations (DNS) to study the influence of the rotation ratio a on the flow structures and the corresponding transported angular velocity flux for Ta up to $Ta = 10^8$. Our motivation is twofold: as a first objective, we wish to further investigate the analogy between RB and TC flow by comparing the scaling laws of the global response across the different flow states. Our second objective is to study the optimal transport, which was recently observed in TC experiments (Paoletti & Lathrop 2011; van Gils *et al.* 2011*b*, 2012), by using data obtained from DNS. In DNS we have access to the complete velocity field, which is not available in experiments, and this allows us to study this phenomenon in much more detail. At present, however, in DNS we are restricted to smaller Reynolds numbers compared to the above-mentioned recent experiments.

Figure 2 shows the cases which are simulated, in the (Ta, a), the $(Ta, 1/Ro)$ and the (Re_o, Re_i) parameter space. Note that a higher density of points has been used in places where the response (Nu_ω, Re_w) shows more variation (where Re_w is the wind Reynolds number defined below). All points have been simulated for fixed $\Gamma = 2\pi$ and $\eta = 5/7$ since these are very similar to the parameters of the Twente turbulent Taylor–Couette (T^3C) setup. There is a significant difference, however, as numerically we take periodic boundary conditions in the axial direction, while the T^3C system is closed with solid boundaries at top and bottom which rotate with the outer cylinder.

In § 2 we start with a description of the numerical method that has been used. In § 3 we will discuss the validation and resolution tests that have been performed. In § 4 the global response, in terms of Nu_ω and the wind Reynolds number Re_w, as functions of the angular velocity ratio a will be discussed. In order to understand the global system response we will analyse the coherent structures in § 5 and the boundary layer

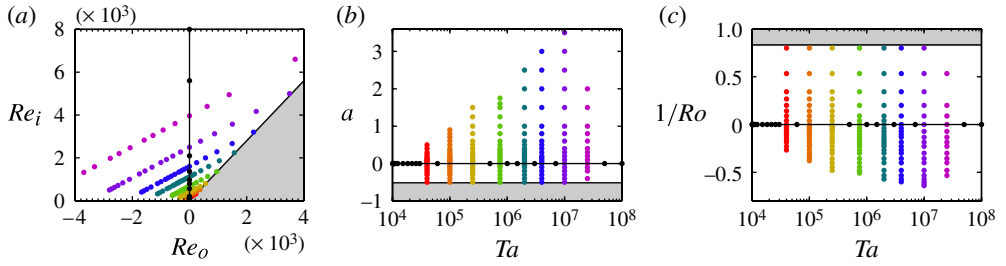

FIGURE 2. (Colour online) Control parameter phase space numerically explored in this paper: (*a*) classical representation (Re_o, Re_i), (*b*) (Ta, a) representation with $a = -\omega_o/\omega_i$, and (*c*) (Ta, $1/Ro$) representation with Ro defined in (2.3). We fixed $\eta = 5/7$, $\Gamma = 2\pi$ and employed axial periodicity. The same colour code (in the online version), denoting the Taylor number, is maintained throughout the paper. The shaded (grey online) area outlines boundary conditions for which the angular momentum of the outer cylinder (L_o) is larger than the angular momentum of the inner cylinder (L_i). This causes the flow to have an overall transport of angular momentum towards the inner cylinder. In this region, the Rayleigh stability criterion applies, which states that if $\mathrm{d}L/\mathrm{d}r > 0$ the flow is linearly stable to axisymmetric perturbations.

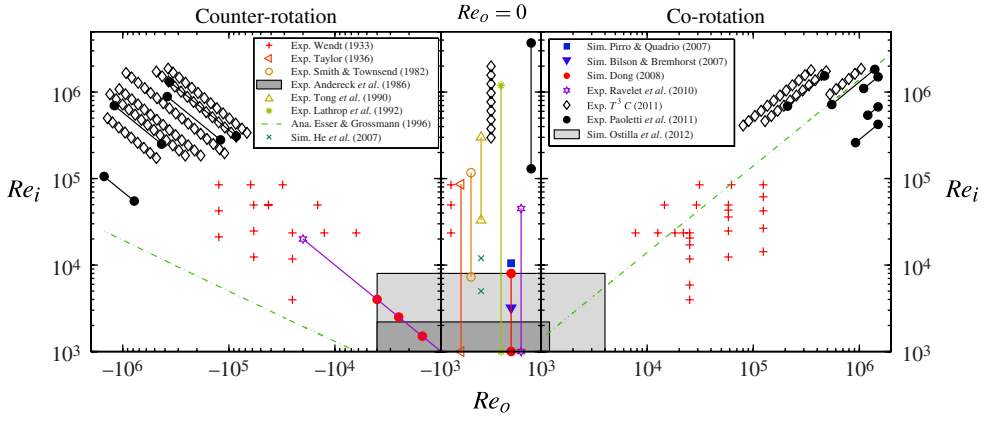

FIGURE 3. (Colour online) Explored phase space (Re_o, Re_i) of TC flow with independently rotating inner and outer cylinders. Both experimental data (Wendt 1933; Taylor 1936; Smith & Townsend 1982; Andereck *et al.* 1986; Tong *et al.* 1990; Lathrop *et al.* 1992*a*; Ravelet, Delfos & Westerweel 2010; Paoletti & Lathrop 2011; van Gils *et al.* 2011*b*) and numerical data (Bilson & Bremhorst 2007; Dong 2007, 2008; Pirro & Quadrio 2008) are shown. Solid lines between markers represent a large density of experiments. The dashed lines are Esser & Grossmann's (1996) estimate for the onset of turbulence with $\eta = 0.71$. The dark shaded area indicates the data points in the well-studied small-Reynolds-number regime of pattern formation and spatial temporal chaos (see e.g. Pfister & Rehberg 1981; Andereck *et al.* 1986; Cross & Hohenberg 1993). The light grey area is the region shown in figure 2(*a*), covered by the present DNS.

profiles in § 6, i.e. quantities that are difficult to analyse in experiments. This allows us to rationalize the position of the maximum in $Nu_\omega(a)$. We conclude with a brief discussion and outlook to future work in § 7.

Brauckmann & Eckhardt (2013) offer a complementary DNS of turbulent Taylor–Couette flow: they employ a spectral code with periodic boundary conditions also in the axial direction and an aspect ratio $\Gamma = 2$ in the axial direction rather

than $\Gamma = 2\pi$ as we do. Also they find a maximum in the angular velocity transport for moderate counter-rotation $a = -\omega_o/\omega_i \approx 0.4$, similar to the experiments by van Gils *et al.* (2011*b*, 2012) and Paoletti & Lathrop (2011) and in the present numerical simulations. So the result seems to be very robust and at least does not strongly depend on Ta, Γ and other details of the flow. Brauckmann & Eckhardt (2013) also offer an analysis of the probability density functions (p.d.f.s) of the local angular velocity fluxes in the different regimes for the inner and outer cylinder, similarly to what has been done for the bulk in the experiments by Huisman *et al.* (2012).

2. Numerical method

The Taylor–Couette flow was simulated by solving the Navier–Stokes equations in a rotating frame, which was chosen to rotate with $\Omega = \omega_o \boldsymbol{e}_z$, where e_z is the unit vector in the direction parallel to the cylinders' axes. In this way the boundary conditions are simplified: at the inner cylinder the new boundary condition is $u_\theta(r = r_i) = r_i(\omega_i - \omega_o)$, while at the outer cylinder we have a stationary wall $u_\theta(r = r_o) = 0$. We can choose the characteristic velocity $U \equiv r_i|\omega_i - \omega_o|$ and the characteristic length scale d to non-dimensionalize the equations and boundary conditions. The characteristic velocity U can be written as

$$U = (\nu/d)\,[8\eta^2/(1+\eta)^3]\,Ta^{1/2}. \tag{2.1}$$

Up to a geometric factor, which is 0.810 for our choice of η, the characteristic velocity U is thus simply $Ta^{1/2}$, expressed in terms of the molecular velocity ν/d. The non-dimensional variables will be labelled with a hat. In this notation, the non-dimensional inner-cylinder velocity boundary condition simplifies to: $\hat{u}_\theta(r = r_i) = (\omega_i - \omega_o)/|\omega_i - \omega_o|$. As $\omega_i - \omega_o$ is positive throughout the range covered in this work, in our coordinate system the flow geometry is simplified to a pure inner-cylinder rotation with the boundary condition $\hat{u}_\theta(r_i) = 1$. The effect of the outer cylinder is felt as a Coriolis force in this rotating frame.

The resulting Navier–Stokes equations in the rotating frame are now

$$\frac{\partial \hat{\boldsymbol{u}}}{\partial \hat{t}} + \hat{\boldsymbol{u}} \cdot \hat{\boldsymbol{\nabla}} \hat{\boldsymbol{u}} = -\hat{\boldsymbol{\nabla}} \hat{p} + \left(\frac{f(\eta)}{Ta}\right)^{1/2} \hat{\nabla}^2 \hat{\boldsymbol{u}} - Ro^{-1} \boldsymbol{e}_z \times \hat{\boldsymbol{u}}, \tag{2.2}$$

where the Rossby number is defined as

$$Ro = \frac{|\omega_i - \omega_o|}{2\omega_o} \frac{r_i}{d} = -\frac{|1+a|}{a} \frac{\eta}{2(1-\eta)} \tag{2.3}$$

and $f(\eta)$ as

$$f(\eta) = \frac{(1+\eta)^3}{8\eta^2}. \tag{2.4}$$

Equation (2.2) is analogous to the Navier–Stokes equation for a rotating Rayleigh–Bénard system,

$$\frac{\partial \hat{\boldsymbol{u}}}{\partial \hat{t}} + \hat{\boldsymbol{u}} \cdot \hat{\boldsymbol{\nabla}} \hat{\boldsymbol{u}} = -\hat{\boldsymbol{\nabla}} \hat{p} + \left(\frac{Pr}{Ta}\right)^{1/2} \hat{\nabla}^2 \hat{\boldsymbol{u}} + \hat{\Theta} \boldsymbol{e}_z - Ro^{-1} \boldsymbol{e}_z \times \hat{\boldsymbol{u}}, \tag{2.5}$$

with the main difference that the Rossby number sign (carried by ω_o in (2.3)) is relevant in TC flow. As long as the transport of angular momentum takes place from the inner to the outer cylinder, i.e. $\omega_i > \omega_o$, Ro is always negative for counter-rotating

cylinders and always positive for co-rotating cylinders. Therefore the sign of Ro affects the flow physics, as it indicates the direction of rotation of the outer cylinder.

These equations were solved using a finite-difference solver in cylindrical coordinates. The domain was taken to be periodic in the axial direction. Coordinates were distributed uniformly in the axial and azimuthal direction. In the radial direction, hyperbolic-tangent-type clustering was used to cluster points near both walls. For spatial discretization, a second-order scheme was used. Time integration was performed fractionally, using a third-order implicit Runge–Kutta method. More details of the numerical method can be found in Verzicco & Orlandi (1996). Large-scale parallelization is obtained with a combination of MPI and OpenMP directives.

In order to quantify the flow, it is useful to continue with the normalized radius $\tilde{r} = (r - r_i)/(r_o - r_i)$ and the normalized height $\tilde{z} = z/(r_o - r_i)$. As an aid to quantification, we define the time- and azimuthally-averaged velocity field as:

$$\hat{\hat{\boldsymbol{u}}}(r, z) = \langle \hat{\boldsymbol{u}}\,(\theta, r, z, t)\rangle_{\theta,t}\,. \tag{2.6}$$

This time- and θ-independent velocity is used to quantify the large-time-scale circulation through the wind Reynolds number:

$$Re_w = \frac{U_w d}{\nu} \quad \text{with } U_w = U\,\langle \hat{\hat{u}}_r^2 + \hat{\hat{u}}_z^2\rangle_{r,z}^{1/2}\,. \tag{2.7}$$

As shown in (2.1), $U \propto Re_i - \eta Re_o$ scales as $Ta^{1/2}$; the non-dimensional transverse velocity fluctuations may or may not lead to corrections of this basic scaling.

The convective dissipation per unit mass can be calculated either from its definition as a volume average of the local dissipation rate for an incompressible fluid

$$\epsilon_u = \nu\,\langle(\boldsymbol{\nabla u})^2\rangle_{V,t} \tag{2.8}$$

or from the global balance (EGL 2007)

$$\epsilon_u - \epsilon_{u,0} = \frac{\nu^3}{d^4}\sigma^{-2} Ta(Nu_\omega - 1), \tag{2.9}$$

where $\epsilon_{u,0}$ is the volume-averaged dissipation rate in the basic, azimuthally symmetric laminar flow, cf. (1.16).

In order to validate the code we have calculated ϵ_u from both (2.8) and (2.9) and checked for sufficient agreement. We define the quantity Δ_ϵ measuring the relative difference:

$$\Delta_\epsilon = \frac{\nu^3 d^{-4}\sigma^{-2} Ta(Nu_\omega - 1) + \epsilon_{u,0} - \nu\,\langle(\boldsymbol{\nabla u})^2\rangle_{V,t}}{\nu\,\langle(\boldsymbol{\nabla u})^2\rangle_{V,t}}. \tag{2.10}$$

Δ_ϵ is equal to 0 analytically, but will deviate when calculated numerically.

The strictest requirement for numerical convergence was that the radial dependence of $Nu_\omega(r)$ had to be less than 1 %. This is a much harder condition to satisfy than torque equality at both inner and outer cylinders, which is satisfied if the Nu_ω at both cylinders is equal. Indeed, in many cases the torques were equal to within 0.01 % but $Nu_\omega(r)$ was not constant within 1 %, which meant either that a higher resolution had to be chosen or that the simulation had to be run for longer time. The time-average of the energy dissipation calculated locally (equation (2.8)) was also checked to converge within 1 %; see § 3.3 for more details.

Re_i	Nu_ω (present study)	Nu_ω (Fasel & Booz 1984)	Nu_ω (Pirro & Quadrio 2008)
60	1.0005	1.0000	1.0000
68	1.0006	1.0000	1.0000
70	1.0235	1.0237	1.0238
75	1.0835	1.0833	1.0834
80	1.1375	1.1371	1.1372

TABLE 2. Nu_ω for low Re_i and $Re_o = 0$, $\Gamma = 2$, $\eta = 1/2$ and rotational symmetry of order four.

3. Code validation

3.1. *Validation against other codes at low Reynolds number*

First of all, the code was validated against numerical results from Fasel & Booz (1984) and Pirro & Quadrio (2008). This comparison was done through Nu_ω measurements at low Re_i, in the range between 60 and 80. Only a quarter of the TC system was used, assuming a rotational symmetry of order four. The aspect ratio Γ was taken as 2, the radius ratio η as 0.5. These geometrical parameters are different from the ones used in the rest of the paper, but they are used here for validation. The resolution of the simulation ($N_\theta \times N_r \times N_z$) was taken as $32 \times 64 \times 64$, the same as in Pirro & Quadrio (2008). The results can be seen in table 2. The values show a match up to three significant figures, or sometimes even higher.

For the two smallest Reynolds numbers, both references obtain the same result, while we obtain a slightly different result. This probably comes from the fact that they measure the torque directly at the inner cylinder, which we then convert to Nu_ω for comparison, while we measure Nu_ω by taking an average value of $J(r)$ and converting this to a value for the torque and thus Nu_ω. The difference between these approaches is probably the origin of the discrepancy. However, as it is very small (below 0.1 %) it is not worrying.

3.2. *Comparison with experiment*

The code was also validated by comparing responses obtained at higher Taylor numbers versus data from Lewis & Swinney (1999). This was done through the Nusselt number for pure inner-cylinder rotation ($a = 0$) at fixed $\eta = 5/7$ and $\Gamma = 2\pi$. The overlap between the simulations and experimental data can clearly be seen in figure 4 in the higher Taylor number range, which we have achieved with the numerics. The shift of about 5 % might be attributed to the difference in both aspect ratio and boundary conditions at the top and bottom because of the vertical confinement in the experiment. As we also have an overlap at the lower Taylor number range with other numerical simulations as shown in § 3.1, we feel sufficiently confident to proceed with our code.

3.3. *Resolution tests*

To achieve reliable numerical results, the grid's temporal and spatial resolution have to be adequate. The requirements for spatial resolution have been studied in Stevens, Verzicco & Lohse (2010) for RB flow. There it was shown that the effect of under-resolved DNS is mainly visible in the convergence of the thermal dissipation rate $\epsilon_\theta = \kappa\langle(\partial_i\Theta)^2\rangle$, which in essence is the thermal Nusselt number Nu. The kinetic dissipation rate $\epsilon_u = \nu\langle(\partial_i u_j)^2\rangle$ turned out to be less sensitive to under-resolution. We

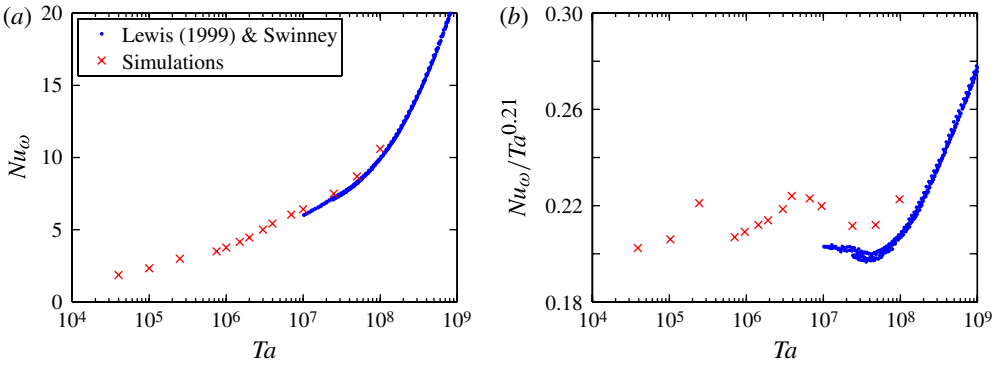

FIGURE 4. (Colour online) (*a*) Absolute (Nu_ω) and (*b*) compensated ($Nu_\omega/Ta^{0.21}$) Nusselt numbers versus Ta for $\eta = 5/7$. Experiments (dots) and the present numerics agree in shape, but there is a slight shift between the data, which we attribute to the different boundary conditions in the lateral direction.

note that even when kinetic dissipation rate has converged within 1 % the simulation can still be under-resolved. It is important to have grid lengths in each direction of the order of the local Kolmogorov or Batchelor lengths.

In TC the corresponding fields to Θ and u are the azimuthal velocity u_θ and the perpendicular components u_r and u_z, respectively. But these are more closely related by the Navier–Stokes equations than the u, Θ fields in RB. Therefore we tested the grid spatial resolution at $a = 0$ by calculating Nu_ω beyond onset of Taylor vortices ($Nu_\omega > 1$) and Δ_ϵ from (2.10), which analytically is equal to 0, checking the (relative) difference between the transport (Nu_ω) and the dissipation rate (ϵ_u). Both were done for different grid resolutions with increasing Taylor number. For all these simulations we took $\Gamma = 2\pi$, $\eta = 5/7$ and $a = 0$. The results are shown in table 3.

Spatial convergence required more grid points than initially expected as satisfying the torque balance alone is a necessary but not a sufficient condition for grid resolution independence. Figure 5(*a,b*) shows graphs of the radial dependence of $Nu_\omega(\tilde{r})$ at $Ta = 2.44 \times 10^5$ ($Re_i = 400$) for an under-resolved case ($100 \times 50 \times 50$, $Nu_\omega = 2.70845$), a reasonably resolved case ($200 \times 100 \times 100$, $Nu_\omega = 2.76208$) and an extremely well-resolved reference case ($300 \times 150 \times 150$, $Nu_\omega = 2.77855$). Nu_ω should not be a function of the radius as mentioned previously, but numerically it does show some dependence. For the under-resolved case we can see that the torque balance is satisfied very well (0.06 %), even if other criteria are not satisfied, e.g. the peak-to-peak variation of Nu_ω is approximately 1 % and the relative error in comparison to the reference case is 2.5 %. The graphs also show that taking the value of Nu_ω at one of the cylinders gives a higher result for the transport current than taking the radial mean.

Figure 5(*c,d*) shows the same plots but for $Ta = 1.91 \times 10^6$ ($Re_i = 1120$) and the three cases: under-resolved ($192 \times 96 \times 96$, $Nu_\omega = 4.8354$), reasonably resolved ($256 \times 128 \times 128$, $Nu_\omega = 4.4600$) and extremely well-resolved reference ($384 \times 192 \times 192$, $Nu_\omega = 4.4776$). For this Taylor number, the under-resolved case shows a smaller deviation of Nu_ω from the mean value and the torque difference in comparison to the lower Taylor number case. However, the discrepancy in the mean value of Nu_ω between the under-resolved and the reference case is much larger (7.9 %). For this Ta the value of Nu_ω at the cylinder walls is larger than the average value of Nu_ω, too.

If we look at the $Nu_\omega(r)$ profiles at given Taylor numbers Ta, they show similar radial dependences, whose magnitudes decrease with increasing resolution. However,

Re_i	Ta	$N_\theta \times N_r \times N_z$	Nu_ω	Δ_ϵ	Case
160	3.90×10^4	$128 \times 64 \times 64$	1.86927	0.0159	R
160	3.90×10^4	$256 \times 128 \times 128$	1.85562	0.0074	S
260	1.03×10^5	$160 \times 80 \times 80$	2.40536	0.0215	R
260	1.03×10^5	$256 \times 128 \times 128$	2.40216	0.0322	S
400	2.44×10^5	$100 \times 50 \times 50$	2.70845	0.0392	U
400	2.44×10^5	$200 \times 100 \times 100$	2.76208	0.0102	R
400	2.44×10^5	$300 \times 150 \times 150$	2.77855	0.0062	S
680	7.04×10^5	$256 \times 128 \times 128$	3.49816	0.0147	R
680	7.04×10^5	$256 \times 128 \times 128$	3.49816	0.0147	T
680	7.04×10^5	$384 \times 192 \times 192$	3.51268	0.0056	S
1120	1.91×10^6	$192 \times 96 \times 96$	4.83540	0.0949	U
1120	1.91×10^6	$256 \times 128 \times 128$	4.46000	0.0174	R
1120	1.91×10^6	$384 \times 192 \times 192$	4.47765	0.0065	S
1600	3.90×10^6	$300 \times 144 \times 144$	5.42553	0.0216	R
1600	3.90×10^6	$432 \times 216 \times 216$	5.37264	0.0063	S
2500	9.52×10^6	$384 \times 192 \times 192$	6.42160	0.0168	R
2500	9.52×10^6	$641 \times 321 \times 321$	6.34068	0.0078	S
3960	2.39×10^7	$641 \times 321 \times 321$	7.46617	0.0161	R
5600	4.77×10^7	$800 \times 400 \times 400$	8.76601	0.0166	R
5600	4.77×10^7	$800 \times 400 \times 400$	8.78178	0.0167	T
8000	9.75×10^7	$1024 \times 500 \times 512$	10.4360	0.0170	R

TABLE 3. Resolution tests for $\eta = 0.714$ and $\Gamma = 2\pi$. The columns display the inner Reynolds number, the Taylor number, the resolution employed, the calculated Nu_ω, the relative discrepancy Δ_ϵ between the two different ways of calculating the energy dissipation, and the 'case': (U)nder-resolved, (R)esolved, (S)patial error reference, and (T)ime error reference, for which the maximum CFL has been halved. The resolution is sufficient for all cases, as the variations are small. Δ_ϵ turns out to be positive; thus the code gives for the dissipation rate a smaller value for the derivatives-squared-based definition than for the Nu_ω-based balance expression.

the shape of this dependence is different for both Taylor numbers. The peaks of $Nu_\omega(r)$ are located close to the boundaries, indicating that they are probably produced by some boundary layer features and are not a systematic bias of our solver.

According to EGL (2007), dissipation should be equal, irrespective of the way in which it is calculated, either directly from its definition or indirectly via the Nusselt number balance, cf. (2.9). Stevens *et al.* (2010) also mentioned the importance of the corresponding equality in RB flow, especially for low values of Pr, as a way to ensure that the flow field is sufficiently resolved and that the gradients are captured adequately. Under-resolving a Taylor–Couette flow will result in a value of Δ_ϵ which is too large in magnitude. This can be seen in table 3 for the under-resolved simulations at $Ta = 2.44 \times 10^5$ and $Ta = 1.91 \times 10^6$. But as was elaborated at the beginning of this subsection, we should consider the convergence of Δ_ϵ towards zero (becoming smaller than any chosen threshold) as a necessary but not as a necessarily sufficient way to ensure grid convergence. Besides Δ_ϵ being small enough, at least $Nu_\omega(r)$ must also be converged.

Sufficient temporal resolution is achieved by using an adaptive time step based on a CFL criterion. If the CFL number is too large, the code destabilizes and the velocities grow beyond all limits. The code used for the simulations employs a third-

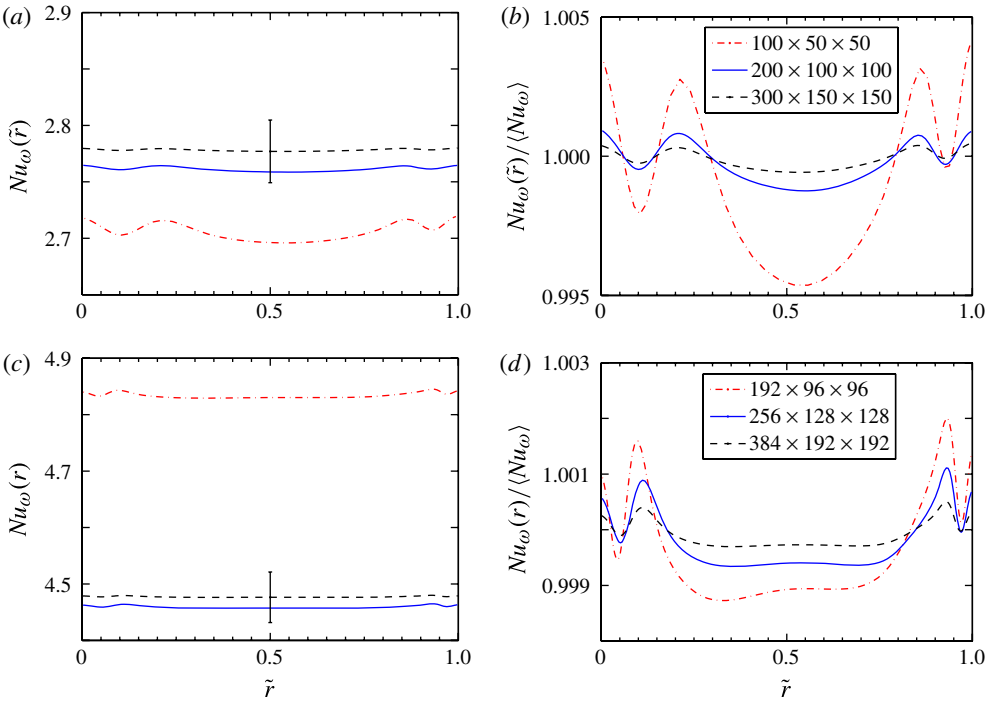

FIGURE 5. (Colour online) Radial dependence of $Nu_\omega(\hat{r})$ for three different grid resolutions (see legends). (*a,b*) $Ta = 2.44 \times 10^5$ and (*c,d*) $Ta = 1.91 \times 10^6$. The figures on the left, (*a,c*), show the absolute values, an error bar indicating a 1 % error for reference. The resolved cases lie within this error bar. The figures on the right, (*b,d*), show the curves normalized by their average value to compare the radial fluctuations of Nu_ω.

order Runge–Kutta time marching algorithm, with a critical CFL number of $\sqrt{3}$. The implicit factorization of the viscous terms may lower this value, so a maximum CFL of 1.4 was taken for safety. This gives a typical time step of $\Delta\hat{t} \sim 10^{-3}$ for the most refined grid, $1024 \times 500 \times 512$ at $Ta = 10^8$, and $\Delta\hat{t} \sim 10^{-1}$ for the coarsest grid, $128 \times 64 \times 64$ at $Ta = 3.90 \times 10^4$.

In order to verify that a CFL number of 1.4 is indeed small enough to ensure that our results are independent of the time step used we performed two simulations with a maximum CFL of 0.7 (see table 3, case T), one in the time-independent regime and one in the time-dependent regime. In the time-independent regime the results obtained with this lower CFL number are identical to the results obtained when using a maximum CFL of 1.4. In the time-dependent regime the difference between the results obtained with maximum CFL of 0.7 and 1.4 is less than the statistically significant variations.

3.4. *Dependence on initial conditions*

For the lower Taylor numbers the flow was started from rest ($\boldsymbol{u} = 0$). The Taylor vortices start forming within a couple of revolutions. After enough time, a steady state with three pairs of Taylor vortices was reached. However, the simulations can also be started from non-resting conditions. Depending on these conditions a different number of vortex pairs can arise. This has a strong influence on both the global and the local response of the system. Once the vortices have formed, they are persistent in

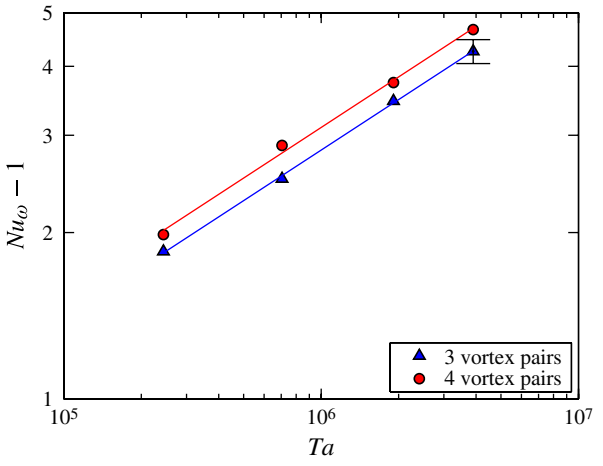

FIGURE 6. (Colour online) Dependence of $Nu_\omega - 1$ versus Ta for pure inner-cylinder rotation on the number of vortices. Although the values of Nu_ω are different, the scaling behaviour with Ta is the same. The error bar indicates a 5 % difference.

time during the simulation. Therefore, it is possible to bias a simulation through the initial conditions to have a higher or lower amount of vortex pairs, which results in a different response.

Although the importance of these coherent structures gets smaller and smaller with increasing Ta (§ 5), at lower Ta the number of vortex pairs must be fixed to determine the response. Brauckmann & Eckhardt (2013) presents an exhaustive study of the effects of the vortex wavelength and number of vortices on Nu_ω for pure inner-cylinder rotation. The study comes to two conclusions, namely that different vortex wavelengths can lead to variations of Nu_ω of up to 20 % at low values of Ta and variations of up to 10 % in Nu_ω at higher values of Ta and that for a fixed vortex wavelength, the number of vortex pairs has no significant effect on Nu_ω.

The study of this parameter will not be repeated here. Instead, a base state, with three pairs of vortices, $N_{pairs} = 3$, has been chosen for all the simulations in this paper. This choice is made to keep the aspect ratio of the vortices as close to 1 as possible ($\lambda_z = \Gamma/2N_{pairs} \approx 1.05$). The effect of having 3 or 4 vortex pairs on the response for selected Ta and pure inner-cylinder rotation is shown in figure 6. A fixed offset can be seen between the two curves. It is important to note that this effect is different from the effect caused by neutral surface stabilization, which occurs when the vortices cannot penetrate the whole flow, and the number of vortices is changed as a result. That will be featured in more detail in § 6.5.

4. Global response

In this section, the global response of the Taylor–Couette system is shown across the parameter space. First the onset of Taylor vortices is analysed. Then the scaling laws are revealed for pure inner-cylinder rotation. Finally, the effect of the outer-cylinder rotation on the scaling laws is investigated and an optimum value of Nu_ω as a function of a for given Ta is found, as has been reported for large Ta from experiments, cf. van Gils *et al.* (2012).

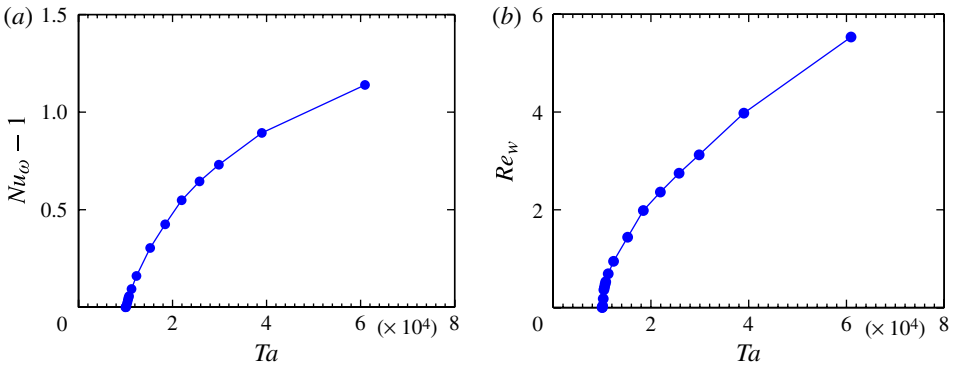

FIGURE 7. (Colour online) System responses $Nu_\omega - 1$ (*a*) and Re_w (*b*) as a function of Ta for pure inner-cylinder rotation near the onset of Taylor vortices. Onset in the present DNS occurs at $Ta \approx 1020$.

4.1. *Transport Nu_ω and wind Re_w for pure inner-cylinder rotation*

The global response of the system is quantified through Nu_ω and Re_w. These two quantities measure two different flow responses. Nu_ω quantifies the transport of angular velocity and Re_w the 'wind', i.e. the additional velocity on top of the azimuthal flow. For the purely laminar–azimuthal flow $Nu_\omega = 1$ by definition, and $Re_w = 0$ as this laminar flow only has an azimuthal velocity component.

First of all we analyse how the onset of Taylor vortices is reflected in the global response quantities Nu_ω and Re_w. $Nu_\omega - 1$ is the additional transport of angular velocity on top of the laminar transport and the wind is the fluid motion on top of the purely laminar–azimuthal flow. Figure 7 shows the numerically calculated $Nu_\omega - 1$ and Re_w as functions of Ta close to onset of the Taylor vortex state. The critical Taylor number (Ta_c) for the onset of Taylor vortices is calculated to be around 1020 for our value of η. This DNS value can be compared with Ta_c as obtained from the analytical approximation of Esser & Grossmann (1996), which is 1038 for the present η. The agreement is within 1.6 %. Later on we shall use these analytically calculated onset Taylor numbers.

After the Taylor vortices have appeared in the system, they are the dominating feature of the flow for several decades of Ta. Figure 8(*a,b*) shows the response of the system with increasing Taylor number in the case of resting outer cylinder and pure inner-cylinder rotation. We plot Nu_ω versus $Ta - Ta_c$ rather than versus Ta as it then shows a better scaling for the points at low Ta.

There seems to be a clear change in the scaling law of Nu_ω versus Ta, but not so in the scaling law for the wind Re_w (figure 8*c,d*). This change occurs between $Ta = 1.91 \times 10^6$ and $Ta = 3.90 \times 10^6$ and has been seen in other numerical simulations too (Coughlin & Marcus 1996). $Nu_\omega - 1$ scales as $(Ta - Ta_c)^{0.34}$ for $Ta < 2 \times 10^6$ and as $Nu_\omega - 1 \sim (Ta - Ta_c)^{0.21}$ for $Ta > 2 \times 10^6$. We attribute the change in scaling to the changes in the coherent flow structures that affect the angular velocity transport but not the global wind amplitude. As will be discussed later in detail, we expect coherent flow structures to lose importance for increasing Ta, see § 5. We note already here that although the loss of influence of coherent structures in RB flow (for $Pr = 1$) and in TC flow sets in at similar values of Ra and Ta respectively, i.e. around 10^7 (Sugiyama *et al.* 2007), there is a large difference in the shear Reynolds numbers Re_s of the boundary layers in these two systems. This will be discussed in the following section.

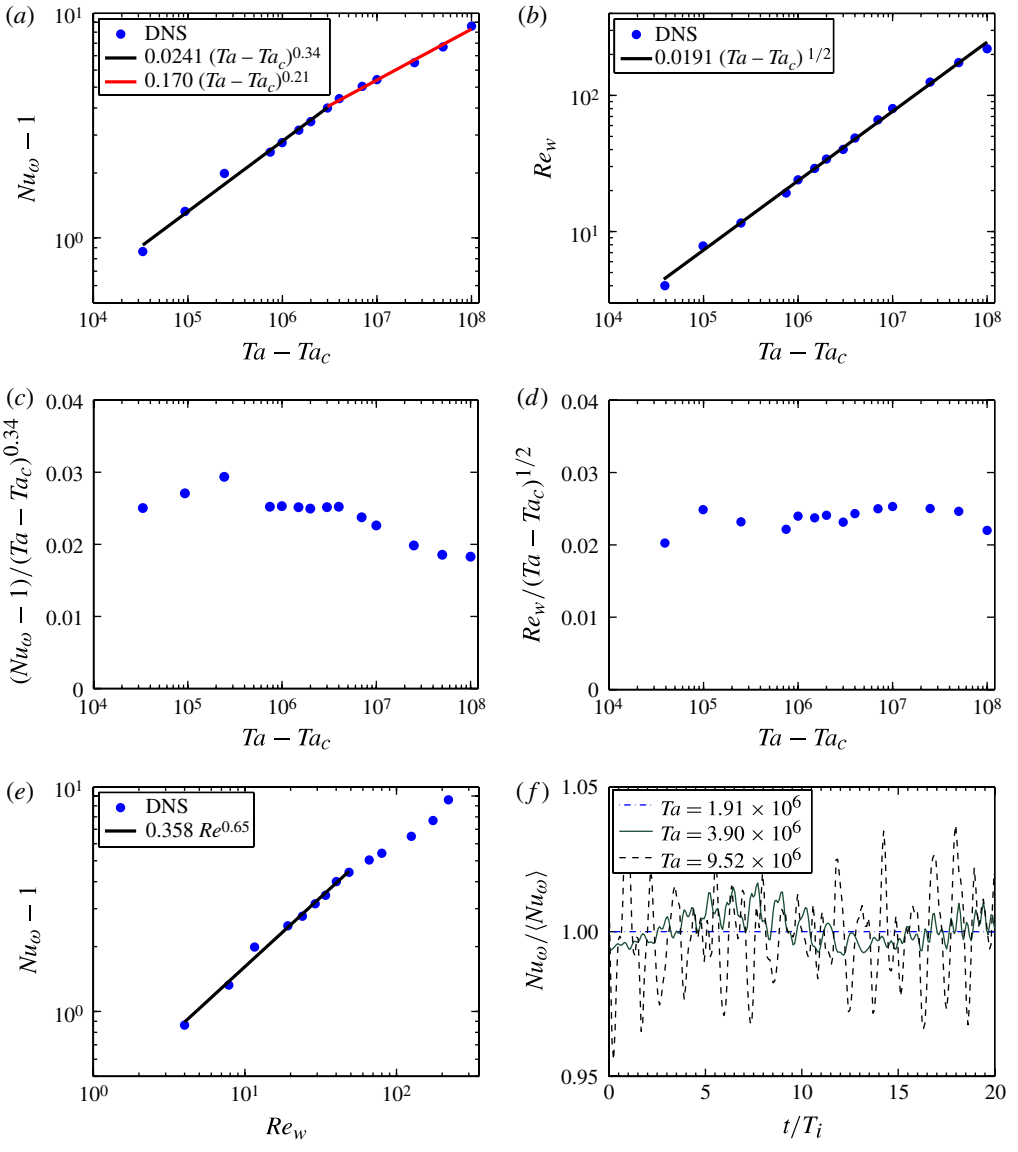

FIGURE 8. (Colour online) (*a,b*) The system response as a function of Ta with best fit lines for pure inner-cylinder rotation, $Nu_\omega - 1$ in (*a*) and Re_w in (*b*). (*c,d*) The data of (*a,b*) compensated by the scaling factor to test the quality of the scaling behaviour. (*e*) The functional relation between the two responses $Nu_\omega - 1$ and Re_w. (*f*) The temporal dependence $Nu_\omega(t)$ for three different Ta. The time dependence can be seen to set in between $Ta = 1.91 \times 10^6$ and $Ta = 3.90 \times 10^6$, just where we see the change in the effective scaling in (*a,c*). The analytical approximation of Esser & Grossmann (1996) is used, i.e. $Ta_c = 1038$ for the present η.

Re_w measures the amplitude (strength) of the Taylor vortices, which persist at long time scales. The non-dimensional characteristic speed of these vortices remains approximately constant with Ta, namely ∼5–6 % of the inner-cylinder velocity u_i,

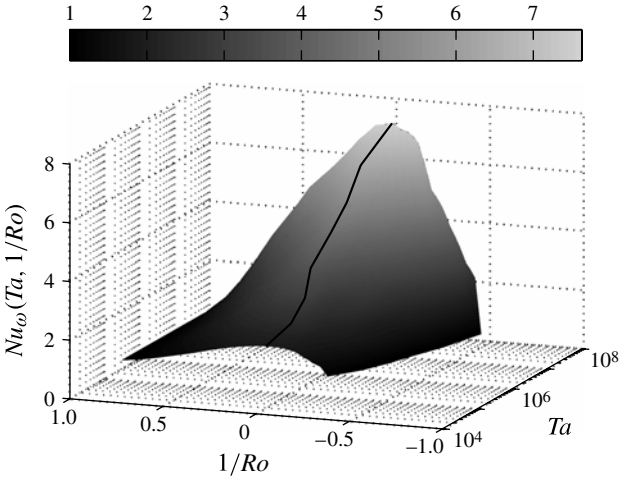

FIGURE 9. $Nu_\omega(Ta, 1/Ro)$. The thick black line shows the position of Ro_{opt}^{-1}, the value of Ro^{-1} for which Nu_ω is maximum at a given Taylor number.

throughout the whole Taylor number range considered, and that is why we see a direct scaling law of $Re_w \sim U \sim (Ta - Ta_c)^{1/2}$, cf. (2.1).

The mutual functional dependence of the two responses Nu_ω and Re_w is presented in figure 8(*e*). As expected from figure 8(*a,b*), the relation between Re_w and Nu_ω also shows the change in the scaling. We interpret this as follows. Before the change, the Taylor vortices are mainly responsible for the additional transport. Beyond the change, some short-time-scale fluctuations appear, indicating other structures, which disrupt the flow and finally become its dominating features, while the Taylor vortices lose importance. In order to see these time scales, we show the temporal dependence of $Nu_\omega(t)$ in figure 8(*f*). The Nusselt number shows almost no time dependence for lower Taylor numbers. But it shows two different time scales at $Ta = 3.90 \times 10^6$. The short time scale gains much more importance for the highest Taylor numbers, causing fluctuations of $\sim$10 %.

4.2. *The effect of outer-cylinder rotation and optimal transport*

In this section the effect of the outer-cylinder rotation on the global responses Nu_ω and Re_w will be studied. This effect is felt by the flow as a Coriolis force (equation (2.2)), so plots in this section will be versus $Ro^{-1} \propto -a/|1+a|$ with $a = -\omega_o/\omega_i$:

$$Ro^{-1} = \frac{2d\omega_o}{U} = -2\frac{1-\eta}{\eta}\frac{a}{|1+a|} = 2\frac{1-\eta}{\eta}\frac{\omega_o}{|\omega_i - \omega_o|}. \tag{4.1}$$

The inverse Rossby number Ro^{-1} runs from $2\eta/(1+\eta)$ to -1 if ω_o runs from $\eta^2\omega_i$, the inviscid Rayleigh-line in the first quadrant of the (Re_o, Re_i)-plane, to $-\infty$. It is useful to note that for a given Ta constant Ro^{-1} means constant a and vice versa. Thus a seems the preferable parameter as it is more direct; Ro^{-1} will be used only when it provides a clear advantage in visualization or later in the paper when we will trace back the occurrence of the maximum to the Navier–Stokes equation.

Figure 9 shows the complete results for Nu_ω as a function of Ro^{-1} and Ta. In order to better quantify the results from figure 9, cross-sectional cuts are taken. By taking cross-sections of constant a, scaling laws can also be discovered for non-zero values

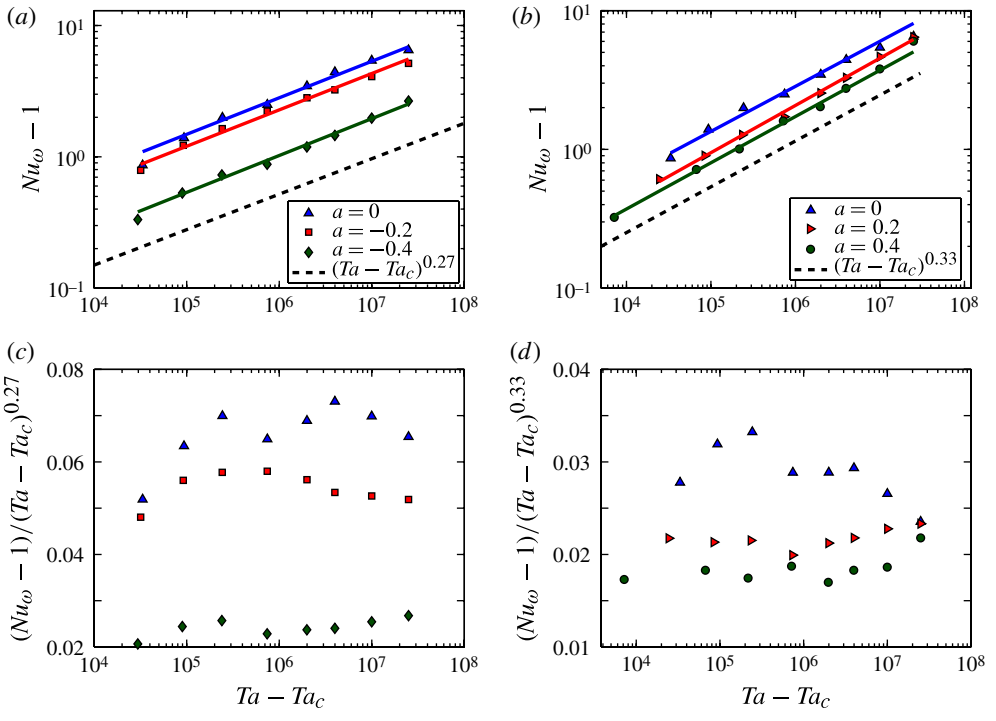

FIGURE 10. (Colour online) $Nu_\omega - 1$ versus $Ta - Ta_c$ for two values of co-rotating a (a) and pure inner-cylinder rotation and two values of counter-rotating a (b). Compensated plots are shown in (c,d). Numerical uncertainties are less than 1 %. Ta_c depends on a and is determined respectively from the analytical approximation (Esser & Grossmann 1996); for $a = 0$ it is $Ta_c = 1038$.

of a, i.e. for co- and counter-rotation $\omega_o \neq 0$. This is shown in figure 10 for five different values of a, two under co-rotation $\omega_o > 0$, two under counter-rotation $\omega_o < 0$, and as reference case $\omega_o = 0$.

For counter-rotating cylinders and Taylor numbers below that at which the change in scaling happens, a universal scaling of approximately $Nu_\omega - 1 \sim (Ta - Ta_c)^{0.34}$ is seen. However, the change in scaling and its exponent happens at lower Ta for $a = 0$, while the scaling prevails to larger Ta for the other a (0.2 and 0.4). The scaling is different for co-rotating cylinders, and is approximately $Nu_\omega - 1 \sim (Ta - Ta_c)^{0.27}$. $Ta_c = 1038$ has been subtracted as done previously so that the scaling is not lost for the first points.

The time independence of Nu_ω is broken for much smaller Ta if the outer cylinder is rotating. For both co- and counter-rotating cylinders time dependence can be noted to set in at Ta as low as 10^5. Also, the scaling of Nu_ω with Ta is maintained throughout a much larger range of the Taylor number. Therefore, the breakdown of time independence can no longer be associated with the change in scaling, as one could conclude when only considering pure inner-cylinder rotation, where the loss of time independence and change in scaling happened at about the same Ta.

Cross-sections of constant Ta are shown in figure 11. $Nu_\omega - 1 = 0$ indicates points for which the flow is purely laminar–azimuthal. For co-rotating cylinders, the maximum value of Ro^{-1} reaches the inviscid Rayleigh stability line $Ro_{Ra}^{-1} = 0.833$ for even the

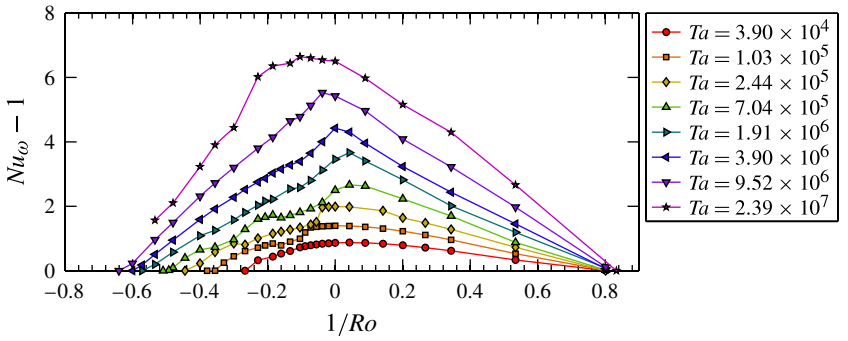

FIGURE 11. (Colour online) $Nu_\omega - 1$ as a function of Ro^{-1} across the available Ta range. The advantage of plotting versus Ro^{-1} can be seen as some of the graphs show piecewise linear behaviour and the value of Ro^{-1} at the inviscid Rayleigh stability limit $a = -\eta^2$ (denoted as Ro_{Ra}^{-1}) is $Ro_{Ra}^{-1} = 0.833$, and appears for all Ta.

lowest values of Ta. On the other hand, the minimum Ro^{-1} which destabilizes the laminar state can be seen to decrease (become more negative) with increasing Ta.

In order to better visualize the results it is useful to define a normalized Nusselt number as $\overline{Nu}_\omega = (Nu_\omega(Ro^{-1}) - 1)/(Nu_\omega(Ro^{-1} = 0) - 1)$, which allows easier visualization of the dependence of Nu_ω on Ro^{-1} across the Ta range of interest. The numerator of $\overline{Nu}_\omega$ goes to zero, if Ro^{-1} becomes too large or too small, i.e. reaches the stability lines (where Nu_ω becomes 1, since the flow is laminar–azimuthal in the stable ranges), while the denominator is always larger than zero, as long as $Ta > Ta_c$.

If Ta is large enough the shape of the graph resembles two straight lines from the maximum value of Nu_ω to Ro_{Ra}^{-1} and Ro_{min}^{-1}. These straight lines have already been seen when plotting Nu_ω versus a slightly different version of Ro^{-1} in Paoletti & Lathrop (2011) and are the reason we chose to plot Nu_ω versus Ro^{-1} in this section.

For smaller Ta an optimum transport for co-rotation can be seen, i.e. for positive values of Ro^{-1}. This holds for Ta less than the discussed change of the scaling behaviour of Nu_ω versus Ta. For the two lowest values of Ta the deviation of Ro^{-1} beyond 0 may still be within numerical uncertainties. However, Ro_{opt}^{-1} is definitely positive for $Ta = 7.5 \times 10^5$ and $Ta = 2 \times 10^6$ and seems to fit with the piecewise linear shape of the graphs. At around $Ta = 4 \times 10^6$, which is beyond the change in scaling, the maximum $\overline{Nu}_\omega$ begins to drift to negative Ro^{-1}, i.e. towards counter-rotation. This can be seen in figure 12. In figure 13 we plotted the positions of the optimum transport in the (Re_o, Re_i) phase space. Clearly, the curve does not have equal distance to the two instability branches of the Esser–Grossmann approximation, as was speculated in van Gils *et al.* (2012). Another feature of the drift of Ro_{opt}^{-1} is the following: while the curve of $\overline{Nu}_\omega$ has a prominent peak at Ro_{opt}^{-1} for values of Ta of around 10^6–10^7, this turns into a plateau for the highest value of Ta and Ro_{opt}^{-1} becomes hard to identify. For the highest value of Ta, the lower boundary Ro_{min}^{-1} already is beyond our parameter range of negative Ro^{-1}.

Experiments (Paoletti & Lathrop 2011; van Gils *et al.* 2011*b*) have found an optimum transport $a_{opt} \approx 0.33$, corresponding to $Ro_{opt}^{-1} \approx -0.20$ for Taylor numbers of the order of 10^{12}. Thus the position of the maximum shifts for higher Taylor numbers.

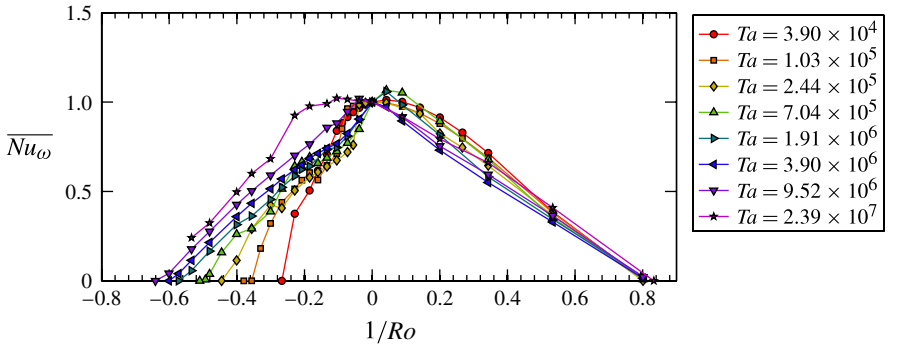

FIGURE 12. (Colour online) $\overline{Nu_\omega}$ versus Ro^{-1}. The shift of Ro_{opt}^{-1} with increasing Ta can be appreciated here.

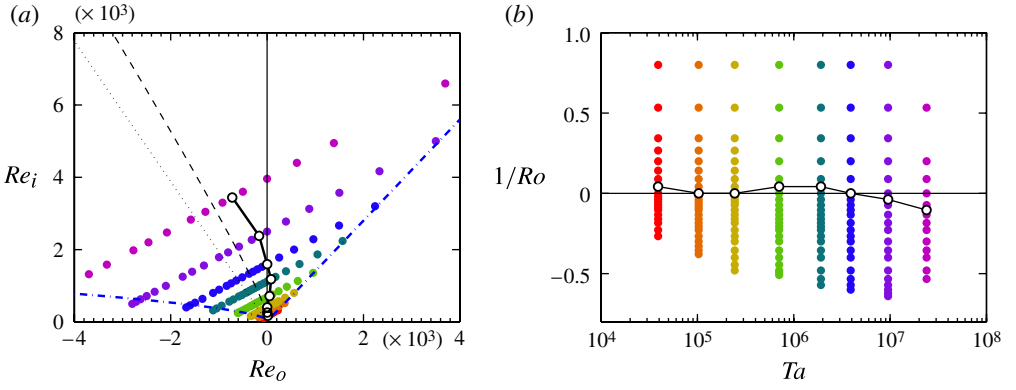

FIGURE 13. (Colour online) Location of the optimal transport (open circles joined by a line) in (*a*) the (Re_o, Re_i) phase space of figure 2(*a*), and (*b*) the $(Ta, 1/Ro)$ phase space of figure 2(*c*). In (*a*), the dash-dot line represents the onset of instability according to Esser & Grossmann (1996) and the dashed line is the line of equal distance to the left and right branch of the Esser–Grossmann instability line. The dotted lines are the bisector of the Rayleigh instability line ($a = -\eta^2$) and the line of pure outer-cylinder rotation ($a = \infty$).

Figures 11 and 12 show some anomalous jumps in the graph around $Ro^{-1} \approx -0.2$ which corresponds to $a \approx 0.3$. These are caused by different vortical states as mentioned in § 3.4. These may be present even if the simulations are started from the same initial conditions for different values of Ro^{-1} and Ta. If the number of vortices is higher, the vortices become stronger, and the value of Re_w, which measures their strength, also becomes higher. Since Nu_ω is monotonically related to Re_w, it also increases. We will further analyse this multi-vortex state in § 6.5.

5. Characterization of the flow state

In this section we will analyse two characteristic Taylor number ranges in TC flow. The first, lower one, is the range in which the importance of coherent flow structures is lost, since these have become too small in size. In § 4 we have observed

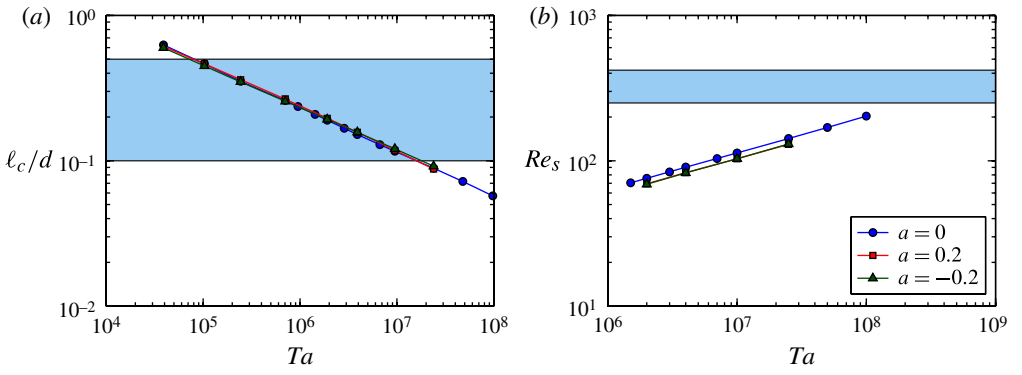

FIGURE 14. (Colour online) (*a*) ℓ_c/d versus *Ta* for $\eta = 5/7$ and three values of a as shown in the legend for (*b*). The shaded region indicates the range of decreasing importance of the coherence structures. (*b*) The shear Reynolds number Re_s of the boundary layers versus *Ta* for the same three a values. In the shaded region we expect a shear instability of the boundary layers, in which the Prandtl laminar boundary layers become turbulent. The TC system then is in the so-called 'ultimate' regime, cf. Grossmann & Lohse (2011).

a change in the scaling law for the angular velocity flux from $Nu_\omega \sim (Ta - Ta_c)^{0.34}$ to $Nu_\omega \sim (Ta - Ta_c)^{0.21}$. Although the Taylor number for this change coincides with the onset of time dependence for pure inner-cylinder rotation, when adding outer-cylinder rotation the onset of the time dependence is much earlier, and a transition in the scaling laws cannot even be seen.

Therefore, the onset of time dependence cannot be linked satisfactorily to the change in the Nu_ω-scaling. Another way of explaining this change is by estimating when the spatially coherent flow structures lose influence because their size becomes too small. We do this by defining an average, global coherence length in terms of the Kolmogorov length scale (Sugiyama *et al.* 2007) resulting from the volume-averaged dissipation rate:

$$\ell_c = 10\eta_K = 10\,(\nu^3/\epsilon_u)^{1/4} = 10d\,(\sigma^{-2}Ta(Nu_\omega - 1) + \hat{\epsilon}_{u,0})^{-1/4} \tag{5.1}$$

where (2.9) has been used for the second equality. We compare the global coherence length ℓ_c with the gap width d or, equivalently with the extent of the remnants of the Taylor vortices, whose length can also be estimated as d, since they tend to have a square aspect ratio.

Figure 14(*a*) shows the variation of ℓ_c/d with increasing Taylor number. The loss of importance of coherent structures happens in the range where ℓ_c/d is between 0.1 and 0.5, corresponding to $Ta \approx 10^6$–10^7. It is just within this *Ta* range where the change in the Nu_ω scaling law occurs. The graph is consistent with that change taking place at approximately the same *Ta* for different values of a, which is what is seen in figure 10. This transition is further analysed in § 6.1.

A second characteristic Taylor number is connected with the shear instability of the boundary layers (BL). Here the laminar Prandtl-type BLs become turbulent. Beyond that *Ta* value the flow is fully turbulent throughout and this state is known as the ultimate state, cf. Grossmann & Lohse (2011). This happens if the BL shear Reynolds number becomes $Re_s > 250$–420, where Re_s is calculated from the shear velocity U_s as

(van Gils *et al.* 2012):

$$Re_s = \frac{U_s \delta}{\nu} = a_{PB}\sqrt{Re_i - Re_w}. \tag{5.2}$$

The empirical constant a_{PB} is taken as 2.3 as in van Gils *et al.* (2012) for Prandtl–Blasius-type BLs in TC flow. This value is obtained by a fit to experimental data, detailed in van Gils *et al.* (2012).

For RB flow this transition is expected at $Ra \approx 10^{14}$ (Grossmann & Lohse 2001; Ahlers *et al.* 2009; Grossmann & Lohse 2011), while figure 14(*b*) shows that the transition in TC is expected for $10^8 \lesssim Ta \lesssim 10^9$. Recently, experiments have confirmed the ultimate scaling both for Nu_ω and Re_w. Huisman *et al.* (2012) have shown that in TC flow $Nu_\omega \sim Ta^{0.38}$ and $Re_w \sim Ta^{0.50}$ when $Ta \gtrsim 10^9$. A confirmation of the analogy between RB and TC is obtained by the high-Ra experiments by He *et al.* (2011) as they measured that $Nu \sim Ra^{0.38}$ and $Re_w \sim Ra^{0.50}$ for $Ra \gtrsim 5 \times 10^{14}$. These measured scaling exponents agree exactly with the predictions by Grossmann & Lohse (2011). In contrast to the experiments of van Gils *et al.* (2011*b*, 2012), in our present numerical simulations the ultimate state has not yet been achieved, as clearly seen from figure 14(*b*).

6. Local results

This section contains the analysis of local results. For convenience we skip in this section the 'hat' on the dimensionless flow field variables, but still understand them as being dimensionless. The angular velocity profiles are shown and the ratio of the BL thickness is calculated and compared with the theory of EGL (2007). The angular velocity profiles reflect the interplay of bulk and boundary layers and that of the mean flow and added perturbations. The importance of convective versus diffusive transport is quantified through the bulk slope of the angular velocity profile, and again we will find a maximum as function of a, which we will connect with the maximum in the angular velocity transport Nu_ω.

6.1. *Local coherence length and vortex characterization*

Figure 15 shows the local coherence length calculated from the local dissipation in analogy to (5.1). This figure adds details on where we expect the Taylor vortices to break down. At low Taylor number, the local coherence length is smaller than 0.1 only very near to the wall, where the highest local dissipation takes place. With increasing Taylor number, the highest local dissipation still is near the wall, but the dissipation rate is large enough in the whole domain to break up the dominance of the coherent structures, even if they do not fully disappear but become small enough.

From figures 14–15 we expect coherent structures to break up at Taylor numbers in the range of $Ta \approx 10^6$–10^7. This may at first sight contradict the earlier finding that the scaling of the wind remains constant across the whole Taylor number range studied (cf. § 4), especially as the characteristic wind velocity is defined from a time-averaged field. One might expect that the perturbations destroy the large-scale structures and as a consequence completely modify the wind. In order to analyse this transition in more detail, we investigate the instantaneous velocity fields before and after the breakdown of coherence. For this, vortices will be characterized employing the so-called λ_2-criterion (Jeong & Hussain 1995).

Figures 16(*a*) and 16(*b*) show full three-dimensional isosurfaces of λ_2 for two Taylor numbers, respectively $Ta = 7.04 \times 10^5$ before the transition, and $Ta = 2.39 \times 10^7$,

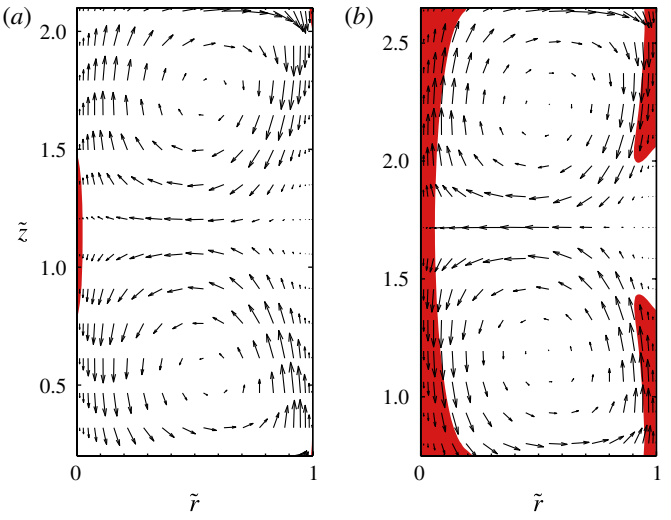

FIGURE 15. (Colour online) The shaded areas show where $\ell_c/d < 0.1$ for pure inner-cylinder rotation and Taylor numbers of: (*a*) $Ta = 1.91 \times 10^6$ and (*b*) $Ta = 9.52 \times 10^6$. In these areas the breakup of the coherent structures is likely to occur. The arrows indicate $\boldsymbol{u}$ in magnitude and direction.

after the transition. Figure 16(*c,d*) shows an azimuthal-cut contour plot of λ_2 for two Taylor numbers. The instantaneous 'wind' is superimposed. It is important to note that for figure 16(*c*) time dependence has not yet set in, so the instantaneous and mean velocity fields are indistinguishable. In this panel we can see that the lowest values of λ_2 are located in the centre of the gap, coinciding with an area of positive u_r wind and almost no u_z wind. Structures of negative λ_2 occupy a significant portion of the space between the cylinders.

On figure 16(*d*), we can see a different picture. The structures of negative λ_2 are now much smaller, and no longer occupy a significant region of the domain, unlike in (*c*). These structures are also in a different place: clustered near the inner cylinder, from where they seem to originate. The instantaneous wind is superimposed on the contour plot. A similar structure as the one in (*c*) is seen, indicating that even though the coherent structures are no longer dominant, the underlying wind behaves in a similar manner. Indeed, once the velocity field is averaged in time, the large-scale Taylor vortices are recovered. This result is consistent with the findings reported by Dong (2007).

6.2. *Angular velocity profiles*

The angular velocity ω is the transported quantity in Taylor–Couette flow. Analysing the dependence of the $\omega(r)$ profiles on the driving parameters *Ta* and *a* seems useful to understand how transport takes place in the flow; $\omega(r)$ profiles are shown in figures 17 and 18. Beyond the breakdown of the laminar, purely azimuthal flow, three distinct regions in the gap appear. These are the inner and outer boundary layers (BL), in which the transport mechanism is dominantly diffusive, and a flatter bulk zone, in which the transport mechanism is dominantly convective, see figure 20(*b*) for a sketch, in which we approximate the profile of the mean azimuthal velocity $\langle \bar{u}_\theta \rangle_z$ by three straight lines, one for each boundary layer and one for the bulk. For the boundary layers, we calculate the slope of the lines by fitting (least mean square) a

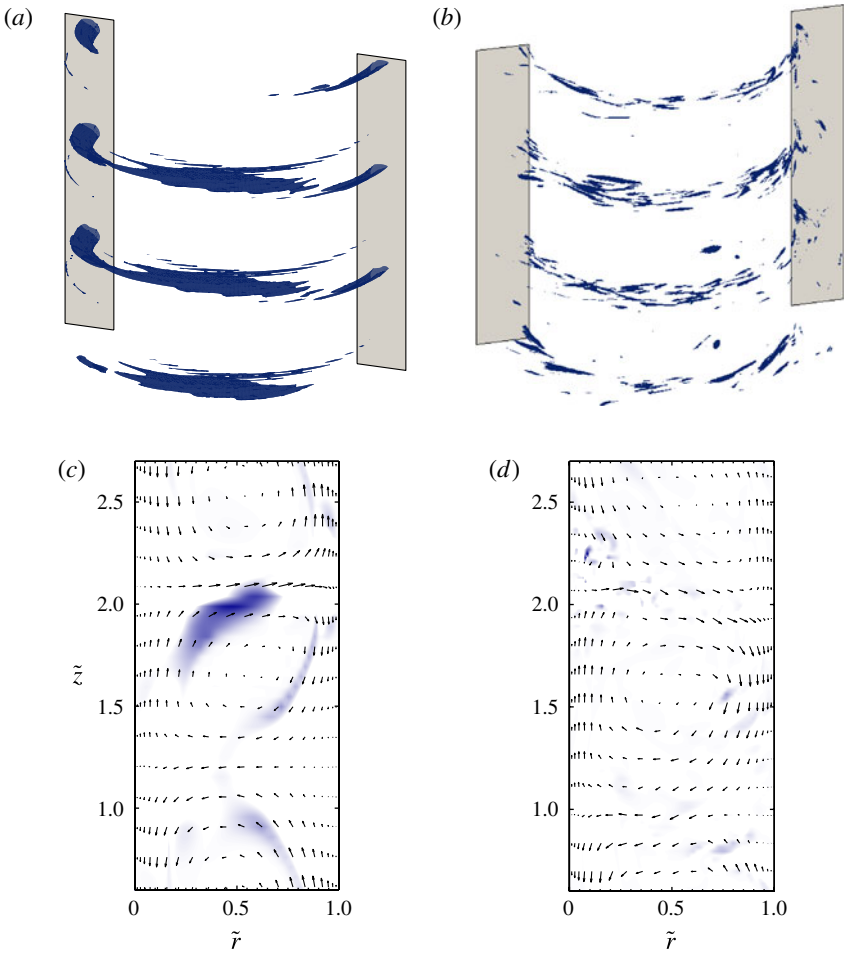

FIGURE 16. (Colour online) (*a,b*) Isosurfaces of λ_2 for pure inner-cylinder rotation and Taylor numbers of: (*a*) $Ta = 7.04 \times 10^5$ and (*b*) $Ta = 2.39 \times 10^7$. (*c,d*) Corresponding contour plots of λ_2 truncated for $\lambda_2 > 0$. The darkest shading represents the minimum value of λ_2 in each plot and white represents $\lambda_2 \geqslant 0$. The arrows indicate $\boldsymbol{u}$ in magnitude and direction. The topography of the negative-λ_2 areas changes from large coherent regions in the centre of the gap – indicating Taylor vortices – to small regions near the inner cylinder – indicating hairpin vortices. The underlying wind, however, remains unchanged.

line through the first three computational grid points. For the bulk, we first force the line to pass through the inflection point of the profile (the nearest grid point). Then, its slope is taken from a least-mean-square fit using two grid points on either side of this inflection point. The respective boundary layer line will cross the bulk line at a point which then defines the thickness of that boundary layer.

In the next two subsections we will discuss the BL and bulk regimes separately.

6.3. *Angular velocity profiles and resulting boundary layer thicknesses*

With increasing *Ta*, in order to accommodate the increasing angular velocity transport, the boundary layers become thinner and the ω-slopes steeper. What is striking is the strong asymmetry between the inner BL and the outer BL, which is much thicker.

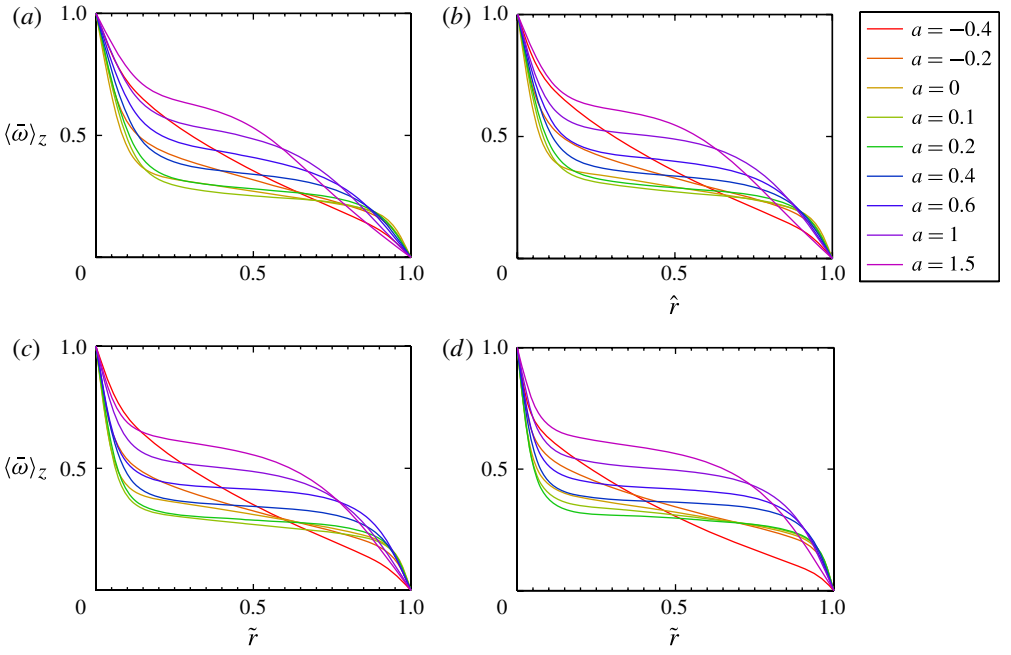

FIGURE 17. The t, θ and also z-averaged angular velocity $\langle\bar{\omega}\rangle_z$ versus $\tilde{r}$ for increasing a and four Taylor numbers: (*a*) 1.91×10^6; (*b*) 3.90×10^6; (*c*) 9.52×10^6; (*d*) 2.39×10^7. The boundary layers of the ω profiles become thinner around slight counter-rotation than they are for higher values of a as well as for co-rotation as an indication of increased transport. For strong co-rotation $a = -0.4$ as well as high a, i.e. strong counter-rotation, at low *Ta* there is not yet a flat bulk zone since the flow is not yet turbulent enough.

Figure 19 shows the ratio between the outer and the inner BL thicknesses versus rotation ratio a for four Taylor numbers. This asymmetry is a consequence of the exact relation $\partial_r\langle\omega\rangle|_o = \eta^3\partial_r\langle\omega\rangle|_i$, obtained from the r-independence of J^ω, cf. (1.4): the slope at the inner cylinder is a factor of η^{-3} larger than at the outer one and thus the outer boundary layer is much more extended than the inner one. Since for the present *Ta*-range the shear Reynolds number Re_s is still below the threshold value range for the transition to turbulence in the boundary layers (see § 5), we can compare the numerically obtained boundary thickness ratio with the one obtained by EGL (2007), which had been derived in the spirit of the Prandtl–Blasius (i.e. laminar-type) boundary layer theory, namely

$$\frac{\lambda_\omega^o}{\lambda_\omega^i} = \eta^{-3}\frac{|\omega_o - \omega_{bulk}|}{|\omega_i - \omega_{bulk}|}. \tag{6.1}$$

Here the value of ω_{bulk} is a characteristic bulk angular velocity chosen to be the value of ω at the inflection point of the ω-profile (see figure 20). It is calculated from the numerical simulations. The result for the BL thickness ratio $\lambda_\omega^o/\lambda_\omega^i$ is shown in figure 19. The agreement with the numerically obtained ratio is satisfactory for the counter-rotating a-cases, getting even better with increasing *Ta*. This is because the estimate is based on a flat profile in the bulk, and indeed the profile becomes flatter with increasing *Ta*. For co-rotation, formula (6.1) apparently fails. This had to

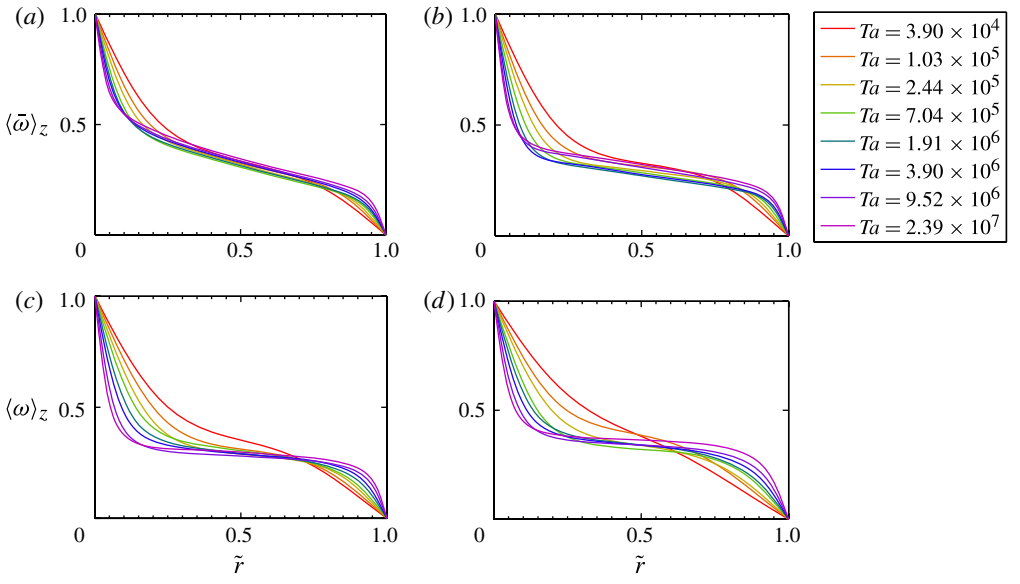

FIGURE 18. $\langle\bar{\omega}\rangle_z$ versus $\tilde{r}$ for increasing Ta and four values of a: (a) -0.2; (b) 0; (c) 0.2; (d) 0.4. The boundary layers for the ω transport become thinner with increasing Ta indicating increased angular velocity transport. The boundary layers get steeper with increasing Ta and the bulk region becomes more extended. For low values of Ta the bulk region is rather small. The $\langle\bar{\omega}\rangle_z$ profile in the centre remains approximately unchanged with Ta.

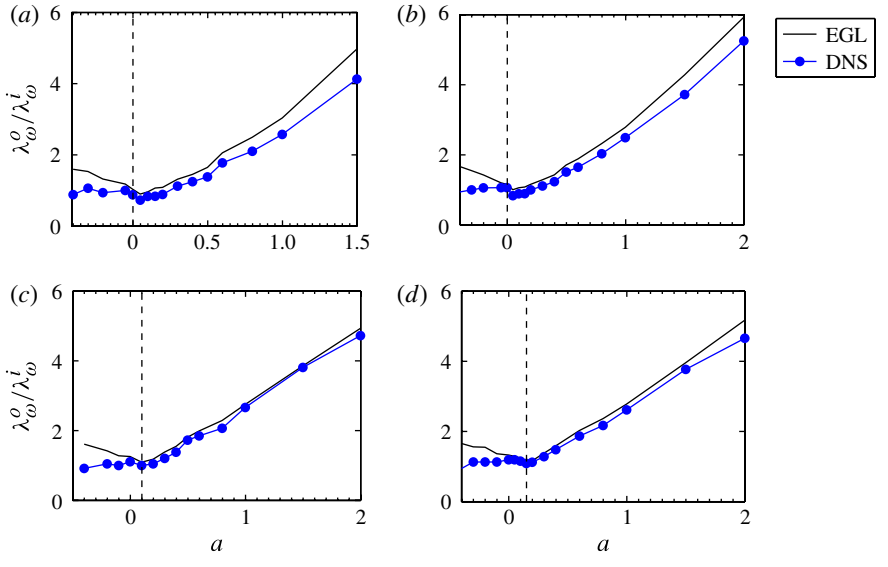

FIGURE 19. (Colour online) Comparison between the present DNS and the theory of EGL (2007) for $\lambda^o_\omega/\lambda^i_\omega$ versus a for four values of Ta: (a) 1.91×10^6; (b) 3.90×10^6; (c) 9.52×10^6; (d) 2.39×10^7. The agreement between theory and simulation is better for counter-rotation and with increasing Ta, but does not match for co-rotation. A dashed line indicates the optimal rotation ratio a_{opt}.

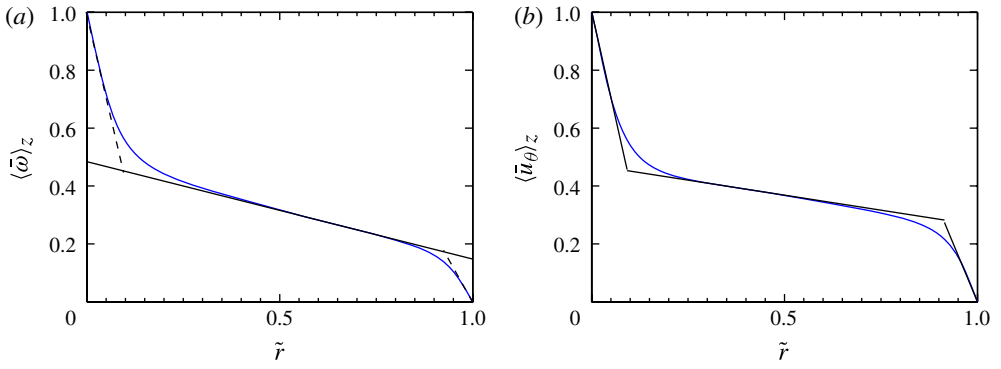

FIGURE 20. (Colour online) Example of the two fitting procedures for $Ta = 1.91 \times 10^6$ and $a = -0.2$: (a) shows a linear fit to the bulk part of the angular velocity $\langle\bar{\omega}\rangle_z$, and ($b$) shows in addition the fit to $\langle\bar{u}_\theta\rangle_z$ for its boundary parts, which will be used in § 6.3. Both bulk fits are done at the inflection point, but for different variables ($\bar{\omega}$ or $\bar{u}_\theta$), which gives a slight difference.

be expected, because the approximation of the profile of $\langle\bar{u}_\theta\rangle_z$ by three straight lines, which was assumed in the derivation of (6.1), is then no longer appropriate.

6.4. *Angular velocity profiles in the bulk*

We now come back to the mean profiles in the bulk. As can be clearly seen from comparing figures 17 and 18, both the mean angular velocity and its slope are controlled by a (or Ro^{-1}) rather than by Ta. This behaviour can be understood from (2.2): the outer-cylinder rotation is reflected in that equation as a Coriolis force. This force is present in the whole domain, while Ta controls the strength of the viscous term, which is dominant in the boundary layer. Therefore the profile is controlled by the Coriolis force, i.e. Ro^{-1} or a, and not by Ta.

To further quantify this, the gradient of $\langle\bar{\omega}\rangle_z$ is calculated. This is done by fitting a straight line to $\langle\bar{\omega}\rangle_z(\tilde{r})$ at the point of the profile's inflection, numerically using the grid points around it. An example of how this is done can be seen in figure 20(a). The results for the profile slopes in the bulk as functions of Ta and a or Ro^{-1} are shown in figure 21.

The graphs collapse on each other for co-rotation ($a < 0$), which is what we expected from figure 18 and our previous analysis. An almost linear relationship between Ro^{-1} and the bulk slope of $\omega(r)$ is found. If pure inner-cylinder rotation ($a = 0$) is approached, the graphs for the various Ta start to diverge and reach a plateau. The absolute value of the slope decreases with increasing Ta. This is due to the increasing importance of convection at higher Ta. Note however that also for this counter-rotating case, for large enough Ta the centre slopes again lose their Ta dependence, i.e. are again mainly controlled by Ro^{-1} and thus the Coriolis term.

We now come back to the co-rotating regime $a < 0$ and want to connect the numerically found approximately linear relationship between the slope of $\omega(r)$ in the bulk and Ro^{-1} with the dynamical equation (2.2), which for the θ-component of the velocity can be rewritten as

$$\partial_t u_\theta + u_r \partial_r u_\theta + \frac{u_\theta}{r}\partial_\theta u_\theta + \frac{u_r u_\theta}{r} + u_z \partial_z u_\theta = -Ro^{-1} u_r - \partial_\theta p. \tag{6.2}$$

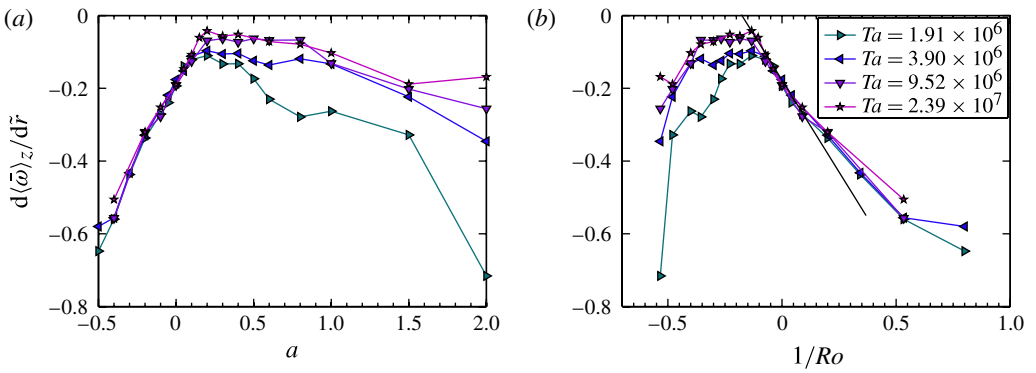

FIGURE 21. (Colour online) The average slope of the angular velocity $\mathrm{d}\langle\bar{\omega}\rangle_z/\mathrm{d}\tilde{r}$ versus a (*a*) and Ro^{-1} (*b*) in the bulk for various Ta. For co-rotation and only slight counter-rotation, there is a nearly linear relationship linking Ro^{-1} with $\mathrm{d}\langle\bar{\omega}\rangle_z/\mathrm{d}\tilde{r}$. A black straight line has been added in this region to artificially extend this relationship up to $\mathrm{d}\langle\bar{\omega}\rangle_z/\mathrm{d}\tilde{r} = 0$. There is also a plateau of $\mathrm{d}\langle\bar{\omega}\rangle_z/\mathrm{d}\tilde{r}$ at counter-rotation. Here the r-slopes are smaller, i.e. the profiles flatter, for increasing Ta, reflecting an increased convective transport.

The linear relationship can be obtained if we assume that the Coriolis force term $Ro^{-1}u_r$ and convective term $u_r\partial_r u_\theta + u_r u_\theta/r$ balance each other, i.e. we assume that the axial, azimuthal, and temporal dependences are small in (6.2), which then boils down to $u_r(\partial_r u_\theta + u_\theta/r) \sim -u_r Ro^{-1}$. Next, we use the fact that the radial velocity component u_r – the wind – in its non-dimensional form is constant in the present Ta-range (cf. § 4, seen also in experiment of Huisman *et al.* 2012). Therefore, and as u_θ hardly depends on Ro^{-1}, an increased Coriolis force can only be balanced by a larger slope $\partial_r u_\theta$. The only alternative is that the wind u_r vanishes altogether, $u_r = 0$, and the flow state returns to the purely azimuthal, laminar case.

To further substantiate this argument, we now decompose the flow field into a (t, θ, z)-averaged mean azimuthal flow component U_θ, depending on the radial position r only, plus fluctuations u', as well as a decomposition of the pressure into a mean pressure P plus the pressure fluctuations p'. Inserting these Reynolds-type decompositions into the radial and azimuthal momentum equations, in which besides U_θ only its r-derivative survives, and ignoring viscosity for now, we arrive at the following equations:

$$\begin{aligned}&\partial_t u_r' + u_r'\partial_r u_r' + \frac{u_\theta'}{r}\partial_\theta u_r' - \frac{U_\theta^2}{r} - \frac{2U_\theta u_\theta'}{r} - \frac{u_\theta'^2}{r} + u_z'\partial_z u_r' \\ &\quad = -\partial_r(P + p') + Ro^{-1}(U_\theta + u_\theta'), \qquad (6.3)\\ &\partial_t u_\theta' + u_r'\partial_r U_\theta + u_r'\partial_r u_\theta' + \frac{u_\theta'}{r}\partial_\theta u_\theta' + \frac{U_\theta}{r}\partial_\theta u_\theta' + \frac{u_r' U_\theta}{r} + \frac{u_r' u_\theta'}{r} + u_z'\partial_z u_\theta' \\ &\quad = -Ro^{-1}u_r' - \partial_\theta p'. \qquad (6.4)\end{aligned}$$

It is important to note that U_r and U_z are both equal to zero, so $u_r = u_r'$ and $u_z = u_z'$. As long as Ro^{-1} is larger than Ro_{opt}^{-1}, we assume that the mean flow contributions alone already balance in (6.3) and (6.4),

$$-\frac{U_\theta^2}{r} \sim -\partial_r P + Ro^{-1}U_\theta, \qquad (6.5)$$

and

$$u_r' \partial_r U_\theta = u_r' \left(r \frac{\mathrm{d}\langle \bar{\omega} \rangle_z}{\mathrm{d}r} + \langle \bar{\omega} \rangle_z \right) \sim -u_r' \left(Ro^{-1} + \frac{U_\theta}{r} \right). \tag{6.6}$$

As in the bulk $r \approx r_a$ is almost constant, the linear relationship $\partial_r \omega \propto \text{const} - Ro^{-1}$ between Ro^{-1} and bulk slope $\mathrm{d}\langle \bar{\omega} \rangle_z / \mathrm{d}\tilde{r}$ is obtained.

Figure 21(*b*), displaying this linear relationship, can be used to obtain a quantitative estimate for optimal transport for large Ta. We can see two distinct features in the slope of this $\mathrm{d}\langle \bar{\omega} \rangle_z / \mathrm{d}\tilde{r}$ versus Ro^{-1} curve. There is a plateau, where the value of the slope is linked to Ta (and therefore to the viscous term in the equation of motion), and there is a line to the right of the plateau where the value of $\mathrm{d}\langle \bar{\omega} \rangle_z / \mathrm{d}\tilde{r}$ is independent of Ta and thus linked only to the Coriolis force. From the previous discussion and from the experimental evidence of van Gils *et al.* (2012) we know that optimal transport is linked to the flattest ω-profile. We can interpret the shift of Ro_{opt}^{-1} with Ta as that value of Ro^{-1} where the plateau meets the co-rotation linear relationship, i.e. the flattest possible ω-profile that does not break the large-scale balance discussed before. If Ro^{-1} becomes more negative, the profile would have to become flatter to keep on satisfying the large-scale balance. As this does not happen, the transport decreases for more negative Ro^{-1}.

With increasing Ta, the value of $\mathrm{d}\langle \bar{\omega} \rangle_z / \mathrm{d}\tilde{r}$ at the plateau increases, and the curves cross at a smaller value of Ro^{-1}, which corresponds to a shifted maximum. Eventually, the plateau value of $\mathrm{d}\langle \bar{\omega} \rangle_z / \mathrm{d}\tilde{r}$ will tend to zero as seen in the experiments of van Gils *et al.* (2012), and the co-rotation line will cross the plateau at the x-axis. We can extend the straight line to get an estimate for when this happens and obtain $Ro_{opt}^{-1}(Ta \to \infty) = -0.20$, corresponding to $a_{opt} \approx 0.34$, an estimate consistent with the experimental values $a_{opt} \approx 0.33 \pm 0.05$ of Paoletti & Lathrop (2011) and van Gils *et al.* (2012).

If Ro^{-1} is too negative, $Ro^{-1} < Ro_{opt}^{-1}$, the large-scale balance of (6.6) can no longer be satisfied. This can be seen as the Coriolis force now has values which would require a smaller (or even a negative) value of $\mathrm{d}\bar{\omega}/\mathrm{d}\tilde{r}$ for the balance to hold. Since this is not possible to accommodate, bursts will originate from the outer cylinder towards the inner cylinder, because the flow tries to accommodate a large Coriolis force. These bursts increase in importance until they end up stabilizing parts of the flow, or even the whole flow which will drastically reduces the transport. Therefore, a maximum transport is reached just when the Coriolis force balances the large-scale convective term. If it is further increased, stabilized regions start appearing. This is linked to the appearance of a neutral surface, which is analysed in the next section.

The large-scale balance cannot be satisfied either if Ro^{-1} is too positive. The Coriolis force then requires a value of $\mathrm{d}\bar{\omega}/\mathrm{d}\tilde{r} > 1$ to be balanced through the convective acceleration forces due to the average flow, and this cannot be accommodated. Unlike the previous case, the flow cannot be separated into stable and unstable regions. Instead, this can be linked to the complete disappearance of the radial and axial components of the flow (the so-called wind). This causes Nu_ω to drop to the purely azimuthal value, as seen in figure 11.

6.5. *Neutral surface*

In this subsection, we leave the rotating reference frame, and return to the inertial reference frame to analyse the neutral surface which is defined as that surface where, in the inertial reference frame, ω is zero. This surface only exists for non-negative values of a and coincides with the outer cylinder in the case of pure inner-cylinder

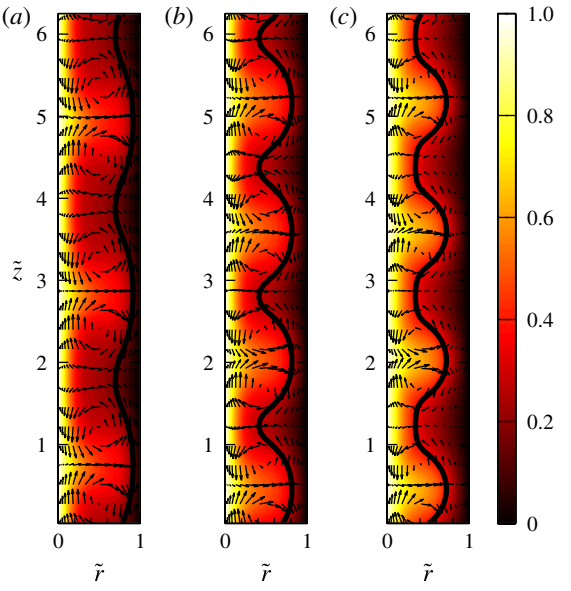

FIGURE 22. (Colour online) Contour plots of the dimensionless angular velocity $\bar{\omega}(\tilde{r}, \tilde{z})$ with indicated neutral surface (black line) for $Ta = 1.03 \times 10^5$. (*a*) $a = 0.2$ and three vortex pairs. (*b*) $a = 0.4$ and four vortex pairs with a non-square aspect ratio and a highly distorted neutral surface. (*c*) $a = 0.6$, four vortex pairs which do not penetrate the whole gap. See also figure 23 for an enlargement.

rotation. In an inertial reference frame, it marks the division between the Rayleigh (inviscid) stable and unstable regions. This means that this surface separates two regions, an unstable inner region and a stable outer region. In the stable region, perturbations to the azimuthal flow (both large-scale wind as in Taylor vortices and small-scale perturbations such as plumes) cannot grow. Therefore we expect this surface to play a significant role in the behaviour of the flow. It was already shown to be important in controlling optimal transport by van Gils *et al.* (2012).

In general, the position r_N of the neutral surface depends on the height z. Figures 22 and 23 and show contour plots of the angular velocity with $r_N(z)$ indicated. Indeed, $r_N(z)$ shows a strong axial dependence, showing heights with positive or negative u_r, at which the neutral surface is pushed more outside or inside, respectively. This strong axial dependence of r_N is a measure for the vortex strength and becomes weaker, when the vortices lose importance at very high Ta. By comparing figures 22 and 24 the effect of the Taylor number on the position of the neutral surface can be seen. Its distortion happens at larger a for increasing Ta, as expected.

If a is large enough, the vortices are no longer able to penetrate the whole gap. There the neutral surface separates the Rayleigh stable and unstable regions. The vortices are mainly located in the unstable range, but partially enter the Rayleigh stable region. Being restricted to part of the gap, they also shrink in the horizontal direction. Because the vortices try to remain as square-like as possible, their height (wavelength) also shrinks, allowing new vortices to appear in the available given height. This is visible in figure 23(*c*). These vortices are also associated with a stronger wind. If the value of a is not very large, they thus will again fill the distance between the two cylinders but with a distorted aspect ratio. A zoom of this effect can

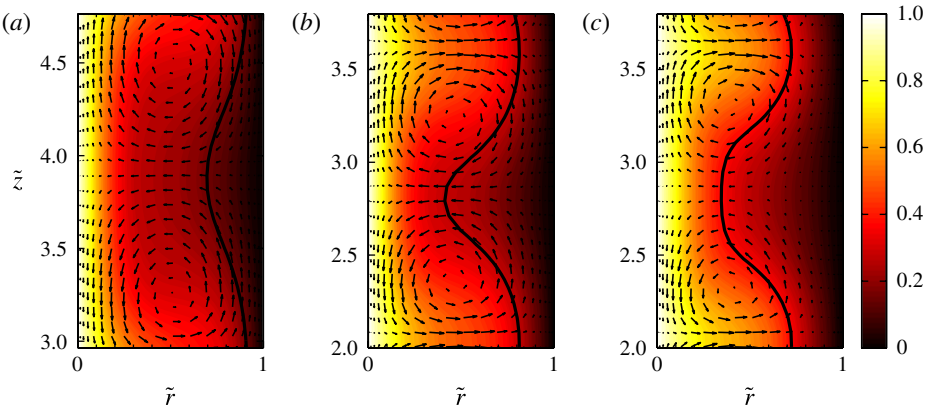

FIGURE 23. (Colour online) Enlarged portions of the contour plots of $\bar{\omega}(\tilde{r}, \tilde{z})$ for $Ta = 1.03 \times 10^5$ with the neutral surface indicated as a black line. (*a*) $a = 0.2$, normal state with three vortices. (*b*) $a = 0.4$, the distorted vortices are strong enough to fully penetrate the gap. (*c*) $a = 0.6$, the distorted vortices cannot penetrate the whole gap due to the stabilizing effects beyond the neutral line. Moreover, with increasing a the distance between the vortex centres shrinks.

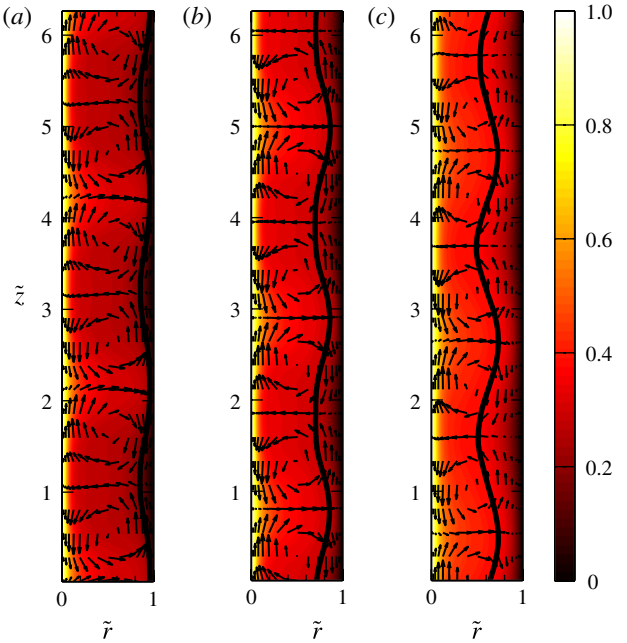

FIGURE 24. (Colour online) Contour plots of $\bar{\omega}(\tilde{r}, \tilde{z})$ with neutral surface indicated for $Ta = 3.90 \times 10^6$ and a-values (*a–c*) of 0.2, 0.4, and 0.6. All of them have three vortex pairs.

be seen in the figure 23(*b*). This causes both the rise in Nu_ω for positive a seen in figure 12 around $a \approx 0.3$ at low Ta and the cross-overs seen in figure 25(*a*) below.

Next, in addition to the temporal and azimuthal average, we also average $r_N(z)$ in the axial direction and call this average $\bar{r}_N$. Figure 25(*a*) shows how $\bar{r}_N$ varies with

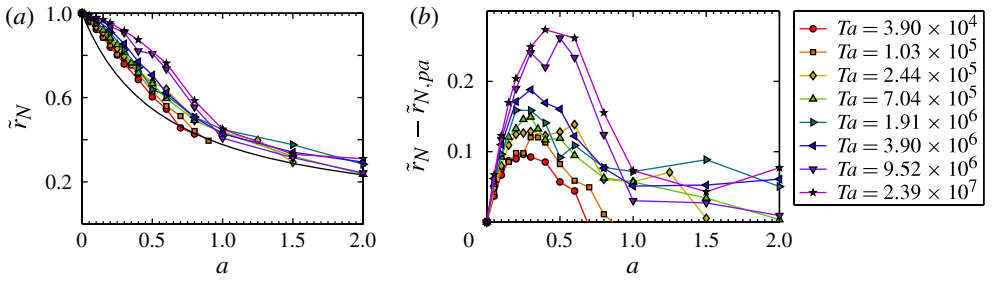

FIGURE 25. (Colour online) (*a*) The neutral surface location $\tilde{r}_N$ of the time, azimuthally, and axially averaged angular velocity versus rotation ratio a for various Ta. The neutral radius $\tilde{r}_N$ is moving inwards with increasing counter-rotation (increasing a), but is pushed back to the towards the outer cylinder for increasing Ta at given a. The black line shows the position of neutral radius $\tilde{r}_{N,pa}$ in laminar, purely azimuthal flow. (*b*) $\tilde{r}_N - \tilde{r}_{N,pa}$ is shown, quantifying the pushing of the neutral line towards the outer cylinder with increasing Ta.

a and Ta. The position of the neutral surface for the laminar, purely azimuthal flow is plotted for comparison. For slight counter-rotation and fixed a, the mean neutral surface is increasingly pushed towards the outer cylinder with increasing Ta due to enhanced turbulence. On the other hand, with increasing a the Coriolis force pushes the neutral surface more and more towards the inner cylinder. Once the neutral surface reaches the laminar and purely azimuthal flow value, the flow is stabilized.

The curves $\tilde{r}_N(a)$ for different Ta can also cross. At a constant rotation ratio, some of the lower Ta curves have a neutral surface which is further away from the inner cylinder than for some of the higher Ta ones. This is due to changes in the number and strengths of vortex pairs in the flow, which happen earlier for lower Ta. With a further increase of a the trend reverses again, since respectively smaller values of a stabilize the flow at already lower Ta. In an inertial reference frame, this simply means that there is no longer a radial velocity which can push the neutral surface outwards, so $\tilde{r}_N$ falls back to the laminar, purely azimuthal flow value, $\tilde{r}_{N,pa} = (\eta)/(1-\eta)(\sqrt{((1+a)/(\eta^2-\mu))} - 1)$

7. Conclusions

An extensive direct numerical simulation (DNS) exploration of the parameter space of a Taylor–Couette (TC) system at Taylor numbers in the range of $10^4 < Ta < 10^8$ is presented. First the code was validated versus existing numerical and experimental data. After this, the transition from the laminar but still purely azimuthal regime to the Taylor vortex state was analysed. The regime where these vortices dominate the flow was studied in detail, revealing scaling laws between the Taylor number Ta, the angular velocity flux $Nu_\omega - 1$, and the wind Reynolds number Re_w. These scaling laws ceased to be valid when the Taylor number was increased beyond $Ta \approx 3 \times 10^6$. At this driving strength the coherence structures become so small that they lose importance and are no longer the dominating feature of the flow.

Then the effect of the outer-cylinder rotation on these scaling laws was analysed. If both cylinders are co-rotating, the scaling laws were (slightly) modified, but for counter-rotating cylinders no significant differences could be seen. After the shrinking of the coherent structure and loss of their importance the value for optimal transport

a_{opt} shifted towards counter-rotation. This drift is expected to continue at higher Taylor numbers and will be the subject of future DNS investigations.

Next, the behaviour of local flow variables was studied. Analysing the profiles $\omega(r)$ sheds light on the two transport mechanisms, convective and diffusive, cf. the two contributions in (1.4). The optimal transport of ω could be linked to a balance between the Coriolis force and the inertial terms in the equations of motion. This balance is best achieved when the bulk profile is flattest, and is broken with increasing counter-rotation. This leads to the appearance of a neutral line and of 'stabilizing' bursts.

The outer boundary layer of the ω-profile is much thicker than the inner boundary layer. The quality of the approximation of the ω-profiles by three straight lines was found to improve with increasing *Ta*, as the (bulk-) turbulence becomes stronger. But although the bulk is turbulent, the boundary layers are still of Prandtl–Blasius type. TC flow only reaches the ultimate state if the boundary layers also undergo a shear instability and become turbulent, too. The present analysis showed that this transition is expected to happen in the *Ta* range between 10^8 and 10^9, which is just outside the range of the present DNS. It will be analysed in future work.

Our ambition is to further extend the *Ta* range in our DNS of TC flow in order to allow a one-to-one comparison between experiments and simulations in the ultimate regime of TC turbulence and to explore the physics of this ultimate regime, in particular to understand the transition to this regime, and the bulk–boundary layer interaction in that regime. This ultimate regime in TC flow has recently been observed and analysed in the experiments by Huisman *et al.* (2012) and van Gils *et al.* (2012), as well as in Rayleigh–Bénard (RB) experiments of He *et al.* (2011). As the mechanical driving in TC is more efficient than heating in RB convection, it is easier to reach the ultimate regime in TC experiments than in RB experiments. Therefore we expect also numerically to reach the ultimate regime earlier in TC flow than in RB flow.

Acknowledgements

We would like to thank G. Ahlers, H. Brauckmann, B. Eckhardt, D. P. M. van Gils, S. G. Huisman, S. Merbold, E. P. van der Poel, M. Quadrio, and C. Sun for various stimulating discussions during these years. The large-scale simulations in this paper were possible due to the support and computer facilities of the Consorzio interuniversitario per le Applicazioni di Supercalcolo Per Universita e Ricerca (CASPUR) and the Dutch Supercomputing Consortium SARA. We would like to thank FOM, COST from the EU and ERC for financial support through an Advanced Grant.

REFERENCES

AHLERS, G. 1974 Low temperature studies of the Rayleigh–Bénard instability and turbulence. *Phys. Rev. Lett.* **33**, 1185–1188.

AHLERS, G., GROSSMANN, S. & LOHSE, D. 2009 Heat transfer and large-scale dynamics in turbulent Rayleigh–Bénard convection. *Rev. Mod. Phys.* **81**, 503–537.

ANDERECK, C. D., LIU, S. S. & SWINNEY, H. L. 1986 Flow regimes in a circular Couette system with independently rotating cylinders. *J. Fluid Mech.* **164**, 155.

BEHRINGER, R. P. 1985 Rayleigh–Bénard convection and turbulence in liquid-helium. *Rev. Mod. Phys.* **57**, 657–687.

BILSON, M. & BREMHORST, K. 2007 Direct numerical simulation of turbulent Taylor–Couette flow. *J. Fluid Mech.* **579**, 227.

BODENSCHATZ, E., PESCH, W. & AHLERS, G. 2000 Recent developments in Rayleigh–Bénard convection. *Annu. Rev. Fluid Mech.* **32**, 709–778.

BRAUCKMANN, H. & ECKHARDT, B. 2013 Direct numerical simulations of local and global torque in Taylor–Couette flow up to $Re = 30.000$. *J. Fluid Mech.* **718**, 398–427.

BUSSE, F. H. 1967 The stability of finite amplitude cellular convection and its relation to an extremum principle. *J. Fluid Mech.* **30**, 625–649.

CHANDRASEKHAR, S. 1981 *Hydrodynamic and Hydromagnetic Stability*. Dover.

COUGHLIN, K. & MARCUS, P. S. 1996 Turbulent bursts in Couette–Taylor flow. *Phys. Rev. Lett.* **77** (11), 2214–2217.

CROSS, M. C. & HOHENBERG, P. C. 1993 Pattern formation outside of equilibrium. *Rev. Mod. Phys.* **65** (3), 851.

DONG, S. 2007 Direct numerical simulation of turbulent Taylor–Couette flow. *J. Fluid Mech.* **587**, 373–393.

DONG, S. 2008 Turbulent flow between counter-rotating concentric cylinders: a direct numerical simulation study. *J. Fluid Mech.* **615**, 371–399.

DRAZIN, P. G. & REID, W. H. 1981 *Hydrodynamic Stability*. Cambridge University Press.

ECKHARDT, B., GROSSMANN, S. & LOHSE, D. 2007 Torque scaling in turbulent Taylor–Couette flow between independently rotating cylinders. *J. Fluid Mech.* **581**, 221–250.

ESSER, A. & GROSSMANN, S. 1996 Analytic expression for Taylor–Couette stability boundary. *Phys. Fluids* **8**, 1814–1819.

FASEL, H. & BOOZ, O. 1984 Numerical investigation of supercritical Taylor-vortex flow for a wide gap. *J. Fluid Mech.* **138**, 21–52.

GEBHARDT, TH. & GROSSMANN, S. 1993 The Taylor–Couette eigenvalue problem with independently rotating cylinders. *Z. Phys.* B **90** (4), 475–490.

VAN GILS, D. P. M., BRUGGERT, G. W., LATHROP, D. P., SUN, C. & LOHSE, D. 2011*a* The Twente Turbulent Taylor–Couette (T^3C) facility: strongly turbulent (multi-phase) flow between independently rotating cylinders. *Rev. Sci. Instrum.* **82**, 025105.

VAN GILS, D. P. M., HUISMAN, S. G., BRUGGERT, G. W., SUN, C. & LOHSE, D. 2011*b* Torque scaling in turbulent Taylor–Couette flow with co- and counter-rotating cylinders. *Phys. Rev. Lett.* **106**, 024502.

VAN GILS, D. P. M., HUISMAN, S. G., GROSSMANN, S., SUN, C. & LOHSE, D. 2012 Optimal Taylor–Couette turbulence. *J. Fluid Mech.* **706**, 118.

GROSSMANN, S. & LOHSE, D. 2000 Scaling in thermal convection: a unifying view. *J. Fluid. Mech.* **407**, 27–56.

GROSSMANN, S. & LOHSE, D. 2001 Thermal convection for large Prandtl numbers. *Phys. Rev. Lett.* **86**, 3316–3319.

GROSSMANN, S. & LOHSE, D. 2011 Multiple scaling in the ultimate regime of thermal convection. *Phys. Fluids* **23**, 045108.

HAIM, D. & PISMEN, L. M. 1994 Performance of a photochemical reactor in the regime of Taylor–Görtler vortical flow. *Chem. Engng Sci.* **49** (8), 1119–1129.

HE, X., FUNFSCHILLING, D., NOBACH, H., BODENSCHATZ, E. & AHLERS, G. 2011 Transition to the ultimate state of turbulent Rayleigh–Bénard convection. *Phys. Rev. Lett.* **108**, 024502.

HUISMAN, S. G., VAN GILS, D. P. M., GROSSMANN, S., SUN, C. & LOHSE, D. 2012 Ultimate turbulent Taylor–Couette flow. *Phys. Rev. Lett.* **108**, 024501.

JEONG, J. & HUSSAIN, F. 1995 On the identification of a vortex. *J. Fluid Mech.* **285**, 69–94.

KADANOFF, L. P. 2001 Turbulent heat flow: structures and scaling. *Phys. Today* **54** (8), 34–39.

LATHROP, D. P., FINEBERG, J. & SWINNEY, H. S. 1992*a* Transition to shear-driven turbulence in Couette–Taylor flow. *Phys. Rev.* A **46**, 6390–6405.

LATHROP, D. P., FINEBERG, J. & SWINNEY, H. S. 1992*b* Turbulent flow between concentric rotating cylinders at large Reynolds numbers. *Phys. Rev. Lett.* **68**, 1515–1518.

LEWIS, G. S. & SWINNEY, H. L. 1999 Velocity structure functions, scaling, and transitions in high-Reynolds-number Couette–Taylor flow. *Phys. Rev.* E **59**, 5457–5467.

LOHSE, D. & XIA, K.-Q. 2010 Small-scale properties of turbulent Rayleigh–Bénard convection. *Annu. Rev. Fluid Mech.* **42**, 335–364.

LORENZ, E. N. 1963 Deterministic nonperiodic flow. *J. Atmos. Sci.* **20**, 130–141.

PAOLETTI, M. S. & LATHROP, D. P. 2011 Angular momentum transport in turbulent flow between independently rotating cylinders. *Phys. Rev. Lett.* **106**, 024501.

PFISTER, G. & REHBERG, I. 1981 Space dependent order parameter in circular Couette flow transitions. *Phys. Lett.* **83**, 19–22.

PFISTER, G., SCHMIDT, H., CLIFFE, K. A. & MULLIN, T. 1988 Bifurcation phenomena in Taylor–Couette flow in a very short annulus. *J. Fluid Mech.* **191**, 1–18.

PIRRO, D. & QUADRIO, M. 2008 Direct numerical simulation of turbulent Taylor–Couette flow. *Eur. J. Mech. (*B/*Fluids*) **27**, 552.

RAVELET, F., DELFOS, R. & WESTERWEEL, J. 2010 Influence of global rotation and Reynolds number on the large-scale features of a turbulent Taylor–Couette flow. *Phys. Fluids* **22** (5), 055103.

SIGGIA, E. D. 1994 High Rayleigh number convection. *Annu. Rev. Fluid Mech.* **26**, 137–168.

SMITH, G. P. & TOWNSEND, A. A. 1982 Turbulent Couette flow between concentric cylinders at large Taylor numbers. *J. Fluid Mech.* **123**, 187–217.

STEVENS, R. J. A. M., VERZICCO, R. & LOHSE, D. 2010 Radial boundary layer structure and Nusselt number in Rayleigh–Bénard convection. *J. Fluid Mech.* **643**, 495–507.

STROGATZ, S. H. 1994 *Nonlinear Dynamics and Chaos*. Perseus.

SUGIYAMA, K., CALZAVARINI, E., GROSSMANN, S. & LOHSE, D. 2007 Non-Oberbeck–Boussinesq effects in Rayleigh–Bénard convection: beyond boundary-layer theory. *Europhys. Lett.* **80**, 34002.

TAYLOR, G. I. 1936 Fluid friction between rotating cylinders. *Proc. R. Soc. Lond.* A **157**, 546–564.

TONG, P., GOLDBURG, W. I., HUANG, J. S. & WITTEN, T. A. 1990 Anisotropy in turbulent drag reduction. *Phys. Rev. Lett.* **65**, 2780–2783.

VERZICCO, R. & ORLANDI, P. 1996 A finite-difference scheme for three-dimensional incompressible flow in cylindrical coordinates. *J. Comput. Phys.* **123**, 402–413.

WENDT, F. 1933 Turbulente Strömungen zwischen zwei rotierenden Zylindern. *Ing.-Arch.* **4**, 577–595.